

Molecular evolution of early-onset prostate cancer identifies molecular risk markers and clinical trajectories

Clarissa Gerhauser, Francesco Favero, Thomas Risch, Ronald Simon, Lars Feuerbach, Yassen Assenov, Doreen Heckmann, Nikos Sidiropoulos, Sebastian M. Waszak, Daniel Hübschmann, Alfonso Urbanucci, Etsehiwot G. Girma, Vladimir Kuryshev, Leszek J. Klimczak, Natalie Saini, Adrian M. Stütz, Dieter Weichenhan, Lisa-Marie Böttcher, Reka Toth, Josephine D. Hendriksen, Christina Koop, Pavlo Lutsik, Sören Matzk, Hans-Jörg Warnatz, Vyacheslav Amstislavskiy, Clarissa Feuerstein, Benjamin Raeder, Olga Bogatyrova, Eva-Maria Schmitz, Claudia Hube-Magg, Martina Kluth, Hartwig Huland, Markus Graefen, Chris Lawerenz, Gervaise H. Henry, Takafumi N. Yamaguchi, Alicia Malewska, Jan Meiners, Daniela Schilling, Eva Reisinger, Roland Eils, Matthias Schlesner, Douglas W. Strand, Robert G. Bristow, Paul C. Boutros, Christof von Kalle, Dmitry Gordenin, Holger Sültmann, Benedikt Brors, Guido Sauter, Christoph Plass, Marie-Laure Yaspo, Jan O. Korbel, Thorsten Schlomm, Joachim Weischenfeldt

Angaben zur Veröffentlichung / Publication details:

Gerhauser, Clarissa, Francesco Favero, Thomas Risch, Ronald Simon, Lars Feuerbach, Yassen Assenov, Doreen Heckmann, et al. 2018. "Molecular evolution of early-onset prostate cancer identifies molecular risk markers and clinical trajectories." *Cancer Cell* 34 (6): 996–1011.e8. <https://doi.org/10.1016/j.ccell.2018.10.016>.

Molecular Evolution of Early-Onset Prostate Cancer Identifies Molecular Risk Markers and Clinical Trajectories

Clarissa Gerhauser,^{1,32} Francesco Favero,^{2,3,32} Thomas Risch,^{4,32} Ronald Simon,^{5,32} Lars Feuerbach,^{6,32} Yassen Assenov,^{1,32} Doreen Heckmann,^{7,8,32} Nikos Sidiropoulos,^{2,3} Sebastian M. Waszak,⁹ Daniel Hübschmann,^{10,11,12} Alfonso Urbanucci,^{13,14,15} Etsehiwot G. Girma,^{2,3} Vladimir Kuryshv,^{7,8} Leszek J. Klimczak,¹⁶ Natalie Saini,¹⁷ Adrian M. Stütz,⁹ Dieter Weichenhan,¹ Lisa-Marie Böttcher,⁵ Reka Toth,¹ Josephine D. Hendriksen,^{2,3}

(Author list continued on next page)

¹Division of Epigenomics and Cancer Risk Factors, German Cancer Research Center (DKFZ), 69120 Heidelberg, Germany

²Finsen Laboratory, Rigshospitalet, DK-2200, Copenhagen, Denmark

³Biotech Research & Innovation Centre (BRIC), University of Copenhagen, DK-2200, Copenhagen, Denmark

⁴Max Planck Institute for Molecular Genetics, Otto Warburg Laboratory Gene Regulation and Systems Biology of Cancer, Ihnestrasse 63-73, 14195 Berlin, Germany

⁵Department of Pathology, University Medical Center Hamburg-Eppendorf, 20246 Hamburg, Germany

⁶Division Applied Bioinformatics, German Cancer Research Center (DKFZ), Im Neuenheimer Feld 280, 69120 Heidelberg, Germany

⁷Division of Cancer Genome Research, German Cancer Research Center (DKFZ), 69120 Heidelberg, Germany

⁸German Cancer Consortium (DKTK), 69120 Heidelberg, Germany

⁹European Molecular Biology Laboratory (EMBL), Genome Biology Unit, 69120 Heidelberg, Germany

¹⁰Division of Theoretical Bioinformatics, German Cancer Research Center (DKFZ), 69120 Heidelberg, Germany

(Affiliations continued on next page)

SUMMARY

Identifying the earliest somatic changes in prostate cancer can give important insights into tumor evolution and aids in stratifying high- from low-risk disease. We integrated whole genome, transcriptome and methylome analysis of early-onset prostate cancers (diagnosis ≤ 55 years). Characterization across 292 prostate cancer genomes revealed age-related genomic alterations and a clock-like enzymatic-driven mutational process contributing to the earliest mutations in prostate cancer patients. Our integrative analysis identified four molecular subgroups, including a particularly aggressive subgroup with recurrent duplications associated with increased expression of *ESRP1*, which we validate in 12,000 tissue micro-array tumors. Finally, we combined the patterns of molecular co-occurrence and risk-based subgroup information to deconvolve the molecular and clinical trajectories of prostate cancer from single patient samples.

INTRODUCTION

One of the biggest unmet clinical needs in prostate cancer (PC) is to stratify clinically indolent from aggressive types, particularly in

patients diagnosed at young age. Molecular markers have shown promise in risk stratification, but the utility is complicated by the heterogeneous natural history. Primary localized PC develops over decades (Pound et al., 1999), with a typical late

Christina Koop,⁵ Pavlo Lutsik,¹ Sören Matzk,⁴ Hans-Jörg Warnatz,⁴ Vyacheslav Amstislavskiy,⁴ Clarissa Feuerstein,^{1,18} Benjamin Raeder,⁹ Olga Bogatyrova,¹ Eva-Maria Schmitz,¹⁹ Claudia Hube-Magg,⁵ Martina Kluth,⁵ Hartwig Huland,²⁰ Markus Graefen,²⁰ Chris Lawerenz,¹⁰ Gervaise H. Henry,²¹ Takafumi N. Yamaguchi,²² Alicia Malewska,²¹ Jan Meiners,⁵ Daniela Schilling,^{7,23} Eva Reisinger,¹⁰ Roland Eils,^{10,11} Matthias Schlesner,^{10,24} Douglas W. Strand,²¹ Robert G. Bristow,²⁵ Paul C. Boutros,^{26,27} Christof von Kalle,^{8,28} Dmitry Gordenin,¹⁷ Holger Sültmann,^{7,8,33} Benedikt Brors,^{6,29,30,33} Guido Sauter,^{5,33} Christoph Plass,^{1,30,33} Marie-Laure Yaspö,^{4,33} Jan O. Korbelt,^{9,33,*} Thorsten Schlömm,^{20,31,33,*} and Joachim Weischenfeldt^{2,3,9,31,33,34,*}

¹¹Department for Bioinformatics and Functional Genomics, Institute of Pharmacy and Molecular Biotechnology and Bioquant, University of Heidelberg, Heidelberg 69120, Germany

¹²Department of Pediatric Immunology, Hematology and Oncology, University Hospital, Heidelberg 69120, Germany

¹³Centre for Molecular Medicine Norway, Nordic European Molecular Biology Laboratory Partnership, Forskningsparken, University of Oslo, 0316 Oslo, Norway

¹⁴Institute for Cancer Genetics and Informatics, Oslo University Hospital, 0316 Oslo, Norway

¹⁵Department of Core Facilities, Institute for Cancer Research, Oslo University Hospital, 0316 Oslo, Norway

¹⁶Integrative Bioinformatics Support Group, National Institute of Environmental Health Sciences, Durham, 27709 NC, USA

¹⁷Genome Integrity and Structural Biology Laboratory, National Institute of Environmental Health Sciences, Durham, 27709 NC, USA

¹⁸Faculty of Biosciences, Heidelberg University, 69120 Heidelberg, Germany

¹⁹PROGETHER Prostate Cancer Network, 0316 Oslo, Norway

²⁰Martini-Clinic Prostate Cancer Center at the University Medical Center Hamburg-Eppendorf, Martinistrasse 52, D-20246 Hamburg, Germany

²¹Department of Urology, UT Southwestern Medical Center, Dallas, TX 75390-9110, USA

²²Informatics & Biocomputing Program, Ontario Institute for Cancer Research, Toronto, Canada

²³NCT Trial Center, National Center for Tumor Diseases and German Cancer Research Center, 69120 Heidelberg, Germany

²⁴Bioinformatics and Omics Data Analytics (B240), German Cancer Research Center (DKFZ), Heidelberg 69120, Germany

²⁵Manchester Cancer Research Centre, University of Manchester, 555 Wilmslow Road, Manchester, UK

²⁶Ontario Institute for Cancer Research, Toronto, Canada

²⁷Department of Medical Biophysics, University of Toronto, Toronto, Canada

²⁸Division of Translational Oncology, German Cancer Research Center (DKFZ), 69120 Heidelberg, Germany

²⁹National Center for Tumor Diseases (NCT), 69120 Heidelberg, Germany

³⁰German Cancer Consortium (DKTK), 69120 Heidelberg, Germany

³¹Charité Universitätsmedizin Berlin, Charitéplatz 1, D-10117 Berlin, Germany

³²These authors contributed equally

³³Senior author

³⁴Lead Contact

*Correspondence: korbelt@embl.de (J.O.K.), thorsten.schlomm@charite.de (T.S.), joachim.weischenfeldt@bric.ku.dk (J.W.)

age-of-onset (median 66 years of age, seer.cancer.gov). Prior studies have revealed a remarkable inter- and intra-tumor heterogeneity in PC (Boutros et al., 2015; TCGA, 2015) associated with poor outcome in primary localized PC (Espirito et al., 2018). Prior focus on elderly, late-onset patients has hindered the identification of the earliest genomic alterations, which could aid in identifying the evolutionary paths and clinical outcome of PC. One of the earliest molecular alterations in PC are ETS fusions involving the fusion of androgen receptor (AR) responsive promoters and members of the ETS transcription factor (TF) family genes, most notably the *TMPRSS2-ERG* fusion (Tomlins et al., 2005) present in 50% of all PC and exhibiting an elevated occurrence in early-onset PC (EOPC) (Tomlins et al., 2005; Weischenfeldt et al., 2013). PC has relatively few somatic point mutations but has frequent genomic structural variants (SVs), several of which are associated with clinical outcome, including disruption or loss of *PTEN*, *TP53*, *NKX3-1*, and *MAP3K7* (Kluth et al., 2013; Taylor et al., 2010; TCGA, 2015).

Identifying the molecular evolution and clinical trajectories of PC requires analysis of the earliest somatic mutation events. A particular relevant subset of PC are early detected cancers associated with EOPC (Pritchard et al., 2016; Weischenfeldt and Korbelt, 2017; Weischenfeldt et al., 2013), here defined as

patients with an age-at-diagnosis at 55 and below, who are likely to develop a severe disease course and eventually require radical treatment. Studies in EOPC, furthermore, offer insights into early mutational processes and evolutionary trajectories of PC.

RESULTS

Patterns of Somatic Genomic Aberrations in EOPC

We applied uniform and comprehensive genomics-based profiling of 292 PC cases (including 203 EOPCs) (Table S1; Figures 1 and S1A). Profiling included whole genome sequencing (WGS) of tumors and matched peripheral blood from 184 EOPC patients and 85 late-onset (LOPC) patients, methylomes (450k methylome arrays) in 203 EOPC tumors and 45 LOPC tumors and mRNA sequencing (mRNA-seq) of 96 EOPC samples. Established somatic and germline variant calling pipelines were used to identify single-nucleotide variants (SNVs), short insertions and deletions (InDels), and SVs. Genome-wide analysis of somatic SNVs revealed an expected lower average number of SNVs per Mb in EOPC (median = 0.47, interquartile range = 0.49) compared with LOPC (median = 0.53) (Fraser et al., 2017). *TP53* was the most frequently affected gene by nonsynonymous SNVs in the EOPC cohort (6%).

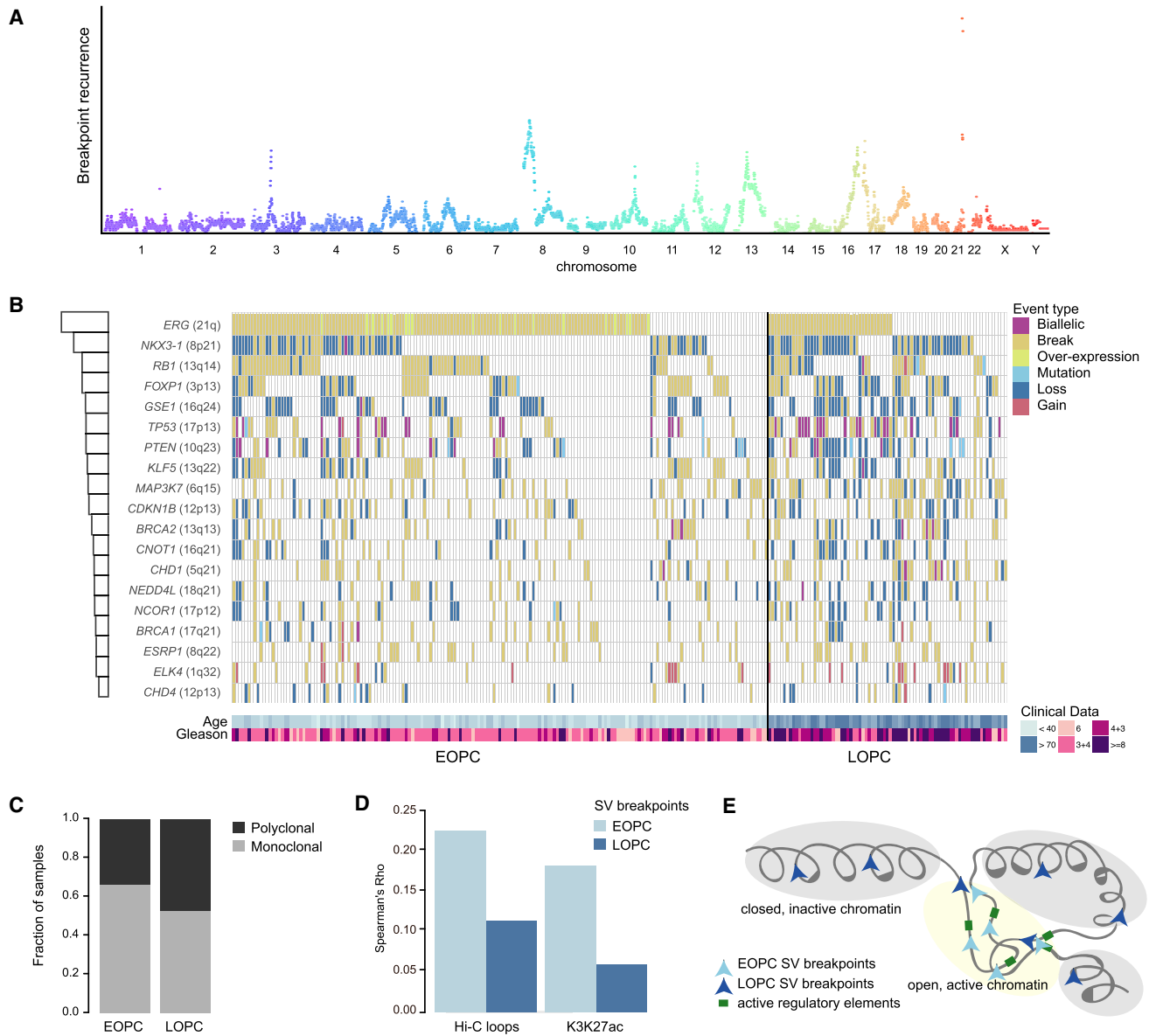


Figure 1. Somatic Alteration Landscape and Age-at-Diagnosis

(A) Genome-wide SV breakpoint recurrence pattern across 292 PC samples, color-coded separately for each chromosome.

(B) An Oncoprint summarizing the mutational landscape of RGA regions in PC, color-coded by the mutational event-type and separate into EOPC and LOPC. The barplot at the left quantifies the recurrence of each RGA in the PC cohort. The patient age and GS are shown at the bottom.

(C) Fraction of EOPC and LOPC tumors from localized PC associated with either clonal or polyclonal paths. $p = 0.18$, chi-square test.

(D) Correlation between breakpoints and Hi-C chromatin loops (combined across eight cell lines) and PC-specific H3K27ac peaks in 1 Mbp bins, separated into localized EOPC and LOPC.

(E) "Chromatin-state" model of age-associated breakpoint patterns in PC.

See also [Figure S1](#) and [Table S1](#).

SVs often involve recurrent fusion gene formation or loss of tumor-suppressor genes in PC (Fraser et al., 2017; Taylor et al., 2010; TCGA, 2015). We confirmed previous findings, namely an increased number of SNVs and SVs with age ($p < 0.001$) (Figures S1B and S1C). We identified recurrent genomic altered loci (RGA), as breakpoint peak regions at minimum 5% recurrence (Figures 1A and 1B). Our analysis revealed 70% of the EOPC tu-

mor genomes carrying an SV associated with formation of an ETS fusion gene (Figure S1D). The second- and third-most frequently altered loci in EOPC were at chromosome 8p (centered at *NKX3-1*, 37%) and 3p14 (centered at *FOXP1*, 30%). We identified *PTEN* as the gene with the highest rate of biallelic inactivation (12 samples) across the cohort, followed by *TP53* (8 samples). Despite being more often affected by

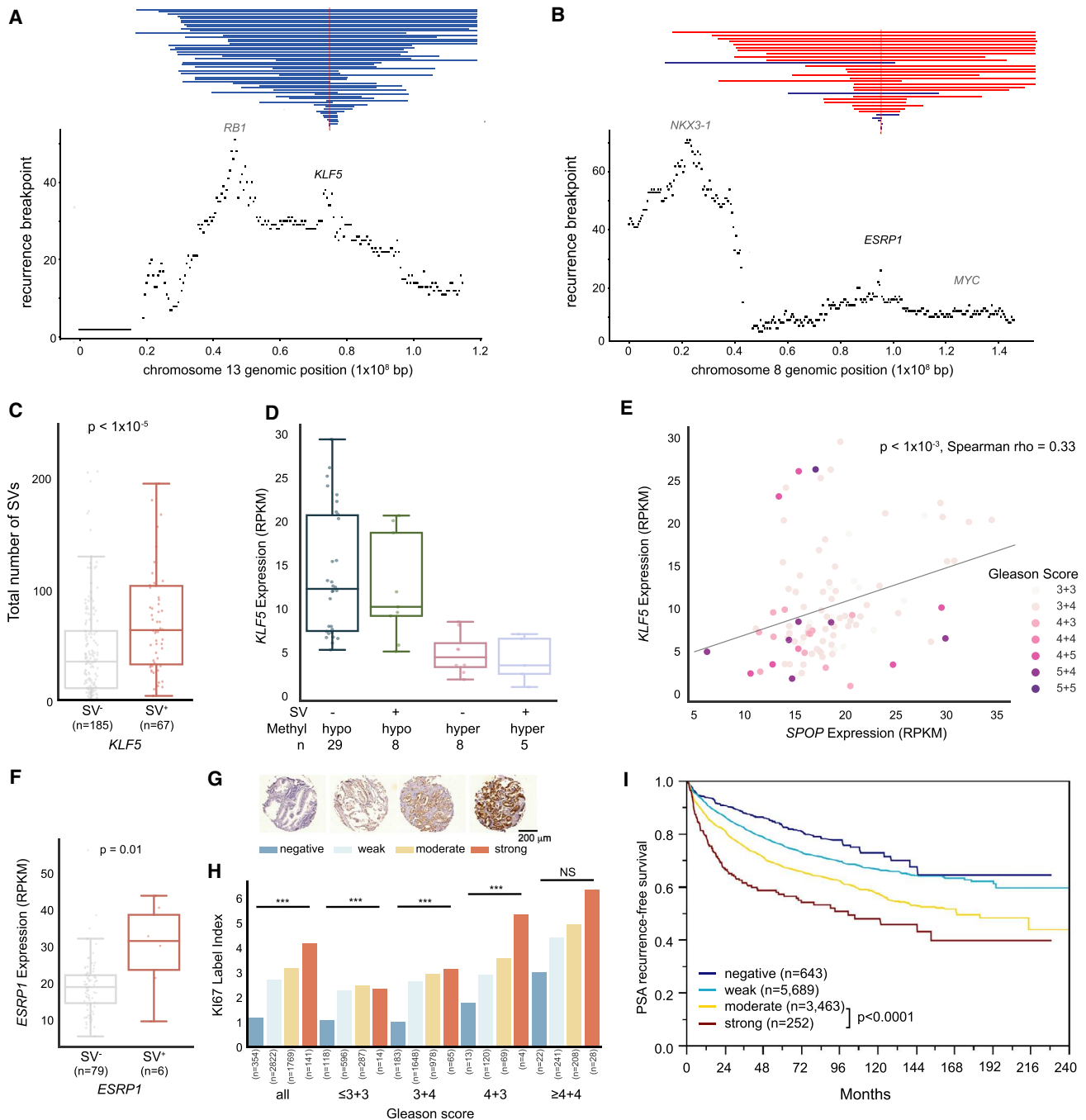


Figure 2. Recurrent Alterations Target *KLF5* and *ESRP1*

(A and B) SV recurrence plot at 13q22 (A) and 8q22 (B) with vertical red and blue lines representing genomic gain and loss, respectively (n tumor samples = 292). The smallest overlapping SV is shown in case of multiple SVs per tumor sample.

(C) Number of somatic SVs from our total cohort of tumors according to presence (SV⁺) or absence (SV⁻) of SVs affecting the *KLF5* locus. MWU-based p value.

(D) *KLF5* gene expression of different methylation and somatic SV states with the x axis representing *KLF5* promoter-proximal methylation status and somatic SV states.

(E) Correlation between *KLF5* and *SPOP* expression, with each dot representing a tumor, color-labeled with GS.

(F) Boxplot of *ESRP1* mRNA expression separated by tumors with an SV gain of *ESRP1* (SV⁺) and without (SV⁻). MWU-based p value.

(G) *ESRP1* protein expression stained in 11,954 tissue microarray samples and scored as “negative” (dark blue), “weak” (light blue), “moderate” (yellow), or “strong” (red).

(legend continued on next page)

SVs, neither *NKX3-1* nor *FOXP1* underwent recurrent biallelic inactivation, corroborating earlier suggestions of haploinsufficient tumor-suppressive roles of these genes (Locke et al., 2012; Myers et al., 2017).

To identify RGAs associated with age-of-onset, we performed a parallel analysis of LOPC genomes, which revealed similar affected loci but with a more uniform pattern, distinct from that of EOPC (Figures S1D and S1E). LOPC displayed an overall higher proportion of RGAs affected by genomic losses compared with a higher rate of balanced breaks in EOPC ($p < 1 \times 10^{-7}$ and $p < 1 \times 10^{-4}$, Fisher's exact test). Moreover, EOPC exhibited a more monoclonal architecture compared with LOPC (66% and 53%, respectively, Figures 1C and S1F), suggesting that EOPC tend to be primarily associated with a clonal origin, potentially due to the shorter life-span compared with LOPC.

The epigenetic landscape is often altered during cancer progression and impacts on where DNA double-strand breaks occur (Aryee et al., 2013; Urbanucci et al., 2017). We previously showed that breakpoints in EOPC genomes occur more often in the vicinity of AR-binding sites (Weischenfeldt et al., 2013). This raises the possibility that age-associated altered chromatin states impact on breakpoint occurrence. We therefore examined genomic breakpoints from EOPC tumors in relation to specific chromatin regions (Taberlay et al., 2014). This revealed a significant enrichment of breakpoints in EOPC near open chromatin, active enhancers, TF binding, and actively transcribed regions (Figures S1G and S1H). Active enhancers are associated with long-range promoter-enhancer DNA-DNA chromatin loops, which can increase the likelihood of SV formation between normally distant loci (Chen et al., 2018). We integrated publicly available Hi-C data, which revealed significant correlation between breakpoints and both the number of chromatin loops and H3K27ac peaks ($p < 0.0001$ both, Spearman's $\rho = 0.23$ and 0.18 , respectively) in EOPC, but to a lesser extent in LOPC ($p < 0.0001$ both, Spearman's $\rho = 0.11$ and 0.06 for Hi-C and H3K27ac, respectively, Figure 1D), suggesting that the chromatin state and long-range interactions partake in shaping the SV landscape in EOPC (Figure 1E).

DNA Rearrangement Recurrence Analysis Identifies a Putative Oncogene Associated with High Cell Proliferation and Poor Outcome

We identified two RGAs in EOPC located at 13q22 (27%) and 8q22 (17%) (Figures 2A and 2B). The minimal overlap peak region at 13q22 centered on *KLF5*, encoding a transcriptional activator involved in repressing cell proliferation (Xing et al., 2014). Loss of 13q22 was associated with decreased *KLF5* mRNA level as well as a global increase in SV and SNV burden (Figures 2C and S2A). We additionally identified a subset of tumors that displayed a marked reduction in *KLF5* expression and a differentially methylated CpG site ($q = 0.002$, t test) proximal to the *KLF5* promoter in a CpG island shore that was inversely corre-

lated with *KLF5* mRNA level (Spearman's $\rho = -0.523$, $q = 0.0038$, CpG no. 18 in Figures 2D and S2B). A recent study in mouse embryonic stem cells identified a set of *KLF5* targets, including the ubiquitin ligase gene *SPOP*, which was significantly downregulated in response to *KLF5* knockdown (Parisi et al., 2010). Chromatin immunoprecipitation sequencing data showed binding of *KLF5* at the *SPOP* promoter (Yan et al., 2013) and we identified a positive correlation between *KLF5* and *SPOP* mRNA levels in our PC cohort (Figures 2E and S2C) as well as in The Cancer Genome Atlas (TCGA) cohort ($p < 1 \times 10^{-4}$, Spearman's $\rho = 0.19$), but no association with the *SPOP* mutation status (Fisher's exact test).

A region at 8q22 displayed recurrent genomic duplications centered on *ESRP1* (Figure 2B), with the minimal overlapping region residing 33 Mbp away from *MYC*. *ESRP1* encodes an RNA-binding protein involved in epithelial-to-mesenchymal transition (EMT) and RNA splicing (Jeong et al., 2017). Tumors harboring duplications intersecting *ESRP1* displayed significantly increased *ESRP1* mRNA expression (>1.5 -fold, Figure 2F). While several duplications overlapped both *ESRP1* and *MYC*, only *ESRP1* displayed a significant increase in mRNA level across the affected samples (Figures 2F and S2D). *ESRP1* duplications were significantly associated with elevated Gleason score (GS) ($p < 1 \times 10^{-11}$, chi-square test), in fact, more than any other RGA in the cohort. We therefore pursued immunohistochemistry-based validation in 11,954 tumor specimens on tissue microarrays (Figure 2G), which confirmed a significant correlation between increased GS and pT and *ESRP1* staining (Figure S2E). High *ESRP1* protein level particularly showed association with high GS ($>4+4$), tumor stage (pT3b-pT4), number of lymph node metastases and preoperative prostate-specific antigen levels. Increased *ESRP1* protein levels correlated with higher proliferation rate irrespective of GS, as measured by Ki67 index labeling (Figure 2H). In addition, *ESRP1* protein intensity was associated with adverse outcome, with strong *ESRP1* staining correlating with significantly shorter time to biochemical recurrence (BCR) (Figures 2I and S2F).

A multivariate analysis revealed *ESRP1* to be an independent prognostic marker in four established clinico-pathological parameters and that high *ESRP1* expression was associated with shorter BCR irrespective of ERG status (Table S2; Figures S2G and S2H). *ESRP1* was particularly discriminative in the biopsy setting, where GS is often underestimated and additional prognostic markers are needed. In summary, we identified recurrent genomic duplications of *ESRP1* associated with increased *ESRP1* protein expression, higher levels of cell proliferation, and elevated GS and tumor stage, and demonstrated that *ESRP1* expression is an independent prognostic biomarker in PC.

Enzymatic Activity Is Associated with the Earliest Detectable Mutational Processes in Prostate Genomes

Mutational signatures can be employed to describe intrinsic and exogenous-mediated mutational processes acting on tumor

(H) Barplot showing Ki67 labeling index separated by GS and *ESRP1* staining. Number of tumors for each category is labeled below each bar. *** $p < 0.001$; NS, not significant ($\alpha = 0.05$, ANOVA-test). The colors of bars correspond to those in (G).

(I) Kaplan-Meier plot, showing prostate-specific antigen (PSA) recurrence-free survival for patients stratified by *ESRP1* staining intensity. Boxplots show median (line), upper, and lower quartiles (boxes), and lines extending to $1.5 \times$ interquartile range (IQR) (whiskers). See also Figure S2 and Table S2.

cells (Alexandrov et al., 2013, 2015; Nik-Zainal et al., 2016) (Figure 3A). We observed six mutational signatures: two clock-like signatures (1 and 5), two related to DNA repair defects (3 and 6), and two related to APOBEC cytidine deaminase-attributable mutagenesis (2 and 13). Mutational processes were associated to GS, in particular the APOBEC signatures (2 and 13) and the homologous recombination repair-associated signature 3 (Figure 3B). The clock-like mutational signatures 1 and 5 were the predominant signatures across all tumors and both showed significant association with patient age (Figure 3C).

Curiously, we also observed clear signs of a clock-like accumulation of APOBEC-associated signature 2 and 13 mutations in PC (Figure 3C), and could further corroborate this finding using a knowledge-based approach that estimates APOBEC mutagenesis in cancer genomes ($p = 5.2 \times 10^{-3}$, Spearman's $\rho = 0.17$). APOBEC proteins are cytidine deaminases that can act to restrict retroelements during the single-stranded DNA replication cycle, but can also induce mutations in cancer genomes (Roberts et al., 2012, 2013). These lesions were previously suggested to be driven by APOBEC3A (A3A) and/or APOBEC3B (A3B) (Swanton et al., 2015). APOBEC-associated mutations occasionally arise as clusters of C strand- (or G strand)-coordinated mutational events (C/G clusters)—also termed kataegis events—a mutational phenomenon resulting in localized hypermutation (Nik-Zainal et al., 2012; Roberts et al., 2012). Indeed, we observed a strong enrichment of APOBEC mutagenesis at C/G clusters in PC (Figure 3D).

We also identified a significant association between patient age and C/G clusters attributable to APOBEC enzymes (Figure S3A), which was primarily attributable to A3B-like mutagenesis at C/G clusters (Figure 3E). To further substantiate the relevance of A3B-like mutagenesis in PC, we genotyped a known ~30 kb germline *APOBEC3B* deletion, which results in complete removal of its protein-coding sequence (Middlebrooks et al., 2016). We observed in germline *APOBEC3B* deletion carriers; (1) significantly fewer APOBEC-associated signature 2 and 13 mutation, (2) reduced expression levels of A3B in PC, and (3) a significant shift from A3B-like to A3A-like mutagenesis (Figure S3B). These findings thus suggest that A3B-like mutagenesis is active at a basal level in prostate cells, and that this endogenous mutagenic process is responsible for the clock-like accumulation of somatic mutations—including the occurrence of localized hypermutation events—in PC. APOBEC-associated mutations have previously been observed to frequently co-localize with SV breakpoints in cancer (Chan and Gordenin, 2015; Roberts et al., 2012). We found a strong enrichment of C/G clusters to co-localize with SV breakpoints compared with both non-coordinated mutation clusters and scattered mutations (Figure 3F), with an increase in co-localization frequency between 1 and 10 kb. Several of these APOBEC-associated SV breakpoints resulted in alteration of driver genes in PC, including formation of *TMPRSS2-ERG* fusion and *PTEN*, *FOXP1*, and *BRCA2* disruption (Table S2). Our findings demonstrate an age-associated mutational process that involves an endogenous mutagenic enzyme, and suggest that mutations attributable to APOBEC enzymes are likely to contribute to the earliest mutations seen in PC patients.

Germline mutations also are likely to contribute to early lesions in PC patients, for example by modulating somatic mutational

processes. Germline protein-truncating variants (PTVs) in DNA damage response (DDR) genes including *BRCA1*, *BRCA2*, *PALB2*, *ATM*, and *CHEK2* have previously been associated with poor outcome and increased frequency of PC metastasis (Na et al., 2017; Pritchard et al., 2016). We detected significant associations between germline PTVs in these DDR genes and somatic SVs and SNVs, as well as APOBEC-like signature 2 and the “BRCAness” mutational signature 3 (Figure 4). In summary, we identify three age-associated mutational processes in PC, namely, CpG mutagenesis, signature 5 with unknown etiology, and A3B-associated mutagenesis. Tumor genomes harboring pathogenic germline mutations in genes involved in homologous recombination repair exhibited increased genomic instability.

PEPCI, a Methylation-Based Risk Score

Normal human prostate tissue is composed of basal, luminal, and stromal cells, whereas PC loses basal cells and gains tumor-specific luminal (T-luminal) cells as well as infiltrating immune cells (Bhasin et al., 2015). Given that DNA methylation profiles are cell type (ct) specific, we sought to account for differences in ct composition in methylation analyses by using available reference methylomes (Teschendorff and Zheng, 2017). To this end, we acquired additional resected samples from benign prostate hyperplasia cases and PC, and performed fluorescence-activated cell sorting to identify the main cts present in PC (STAR Methods) (Figures 5A and S4A–S4C), which enabled us to identify the ct identity of every methylation site in the PC genome.

We found a recurrent shift from basal and luminal cells to T-luminal cells and infiltrating immune cells in high GS tumors (Figures 5B, S4C, and S4D). Given this relevance of T-luminal and immune cell content in identifying high-grade tumors, we combined this information as a Purity-Adjusted Epigenetic Prostate Cancer Index (PEPCI) of tumor aggressiveness (Figures 5A and 5B). We found that high PEPCI was strongly associated with high pT ($p < 1 \times 10^{-7}$, Kruskal-Wallis), high GS ($p < 1 \times 10^{-17}$, Wilcoxon) (Figure 5C) and elevated risk of BCR (log rank $p < 0.0001$). Moreover, PEPCI was able to stratify intermediate-risk (GS7, especially GS4+3) cases (Figures 5D, S4E, and S4F; Table S3), which we validated in the TCGA cohort of primarily LOPC samples (TCGA, 2015) (Figures S4E and S4F; Table S3). Finally, our PEPCI score was also able to independently predict GS and BCR (area under the curve = 0.831 and 0.702, respectively) (Figure S4G). We examined whether particular RGAs were associated with PEPCI-based risk groups (Figure 5E), which revealed a striking association between PEPCI-high and gain of *ESRP1* (odds ratio = 15.7, false discovery rate-corrected $p < 1 \times 10^{-5}$, Fisher's exact test, Table S3).

Integrative Analysis Identifies Molecular Subgroups Associated with Disease Progression

We sought to identify pathways and processes that underwent transcriptional deregulation in EOPC. Using the graph theory-based CLICK algorithm (Sharan et al., 2003) on 96 patients with available mRNA-seq data, we identified seven distinct CLICK clusters (abbreviated CC1-7) of co-expressed genes, splitting the patients into CC-high and CC-low expression groups per CC (Figures 6A and S5A; Table S4). We next

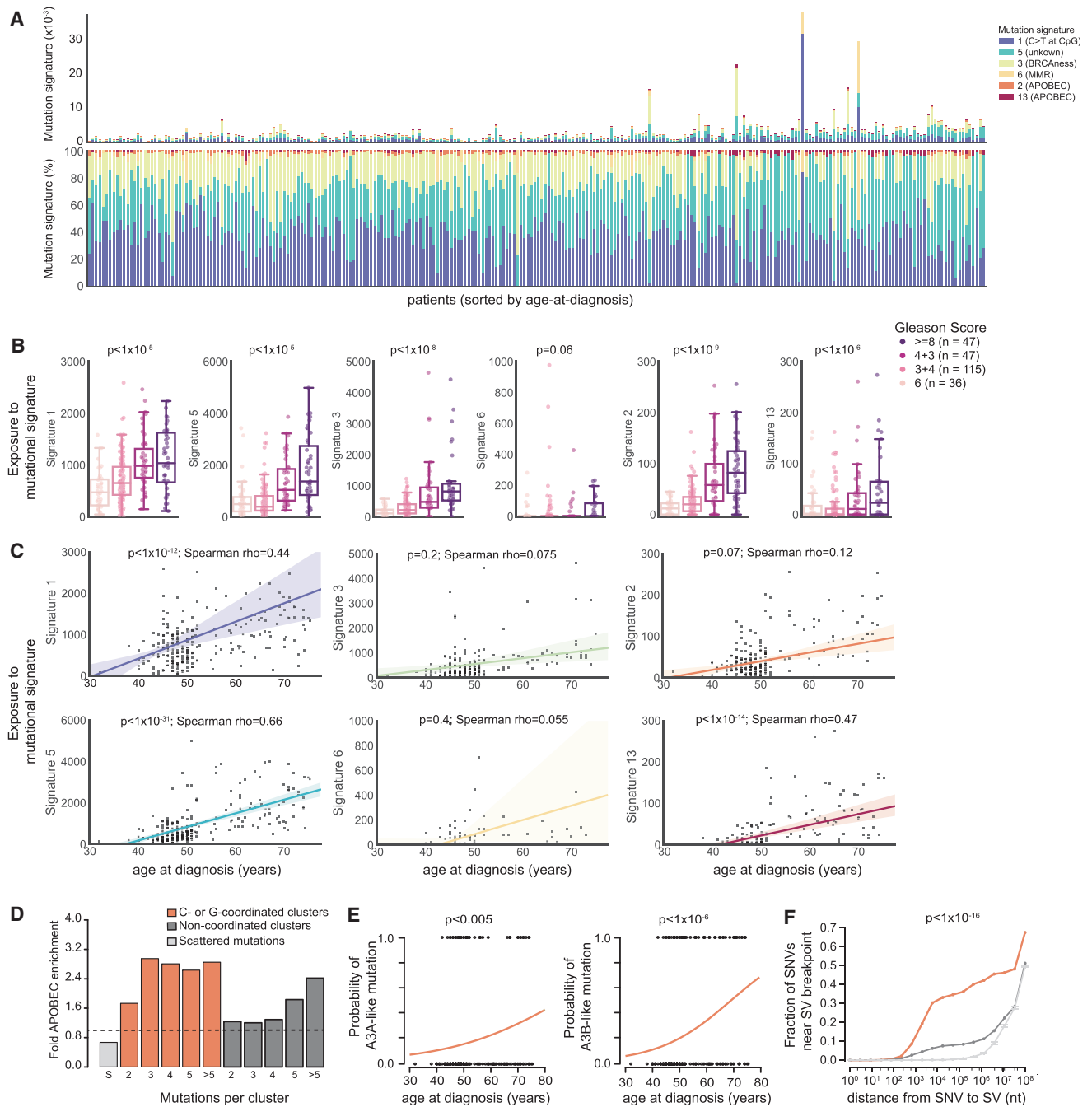


Figure 3. Age-Related Mutational Signatures in Prostate Cancer

(A) Barplot of the absolute (top) and relative (bottom) proportion of exposure of six mutational signatures (1, 5, 3, 6, 2, and 13, colored bars) per individual tumor of patients with localized PC, sorted by age-at-diagnosis (x axis, range from 32 to 75 years).

(B) Association between mutation signature burden (y axis) and GS. POLR p values. Boxplots show median (line), upper, and lower quartiles (boxes), and lines extending to 1.5 × IQR (whiskers).

(C) Correlation between the mutation signature burden and age-at-diagnosis.

(D) Fold-enrichment of APOBEC signature in scattered mutations (light gray), C/G clusters (orange), or non-coordinated clusters (dark gray).

(E) Age-association between A3A ("ytCa" signature, left) or A3B ("rtCa" signature, right) in C/G clusters of mutations as a function of age (binomial logistic regression). Generalized linear model logit p values.

(F) Fraction of mutations close to SV breakpoint for C/G cluster mutations (orange, n = 1,694), non-coordinated cluster mutations (dark gray, n = 8,408), and non-clustered mutations (light gray, 100 bootstraps of 456,406 SNVs, 95% confidence interval shown). The x axis displays log10 distance between SNV and breakpoint.

See also Figure S3.

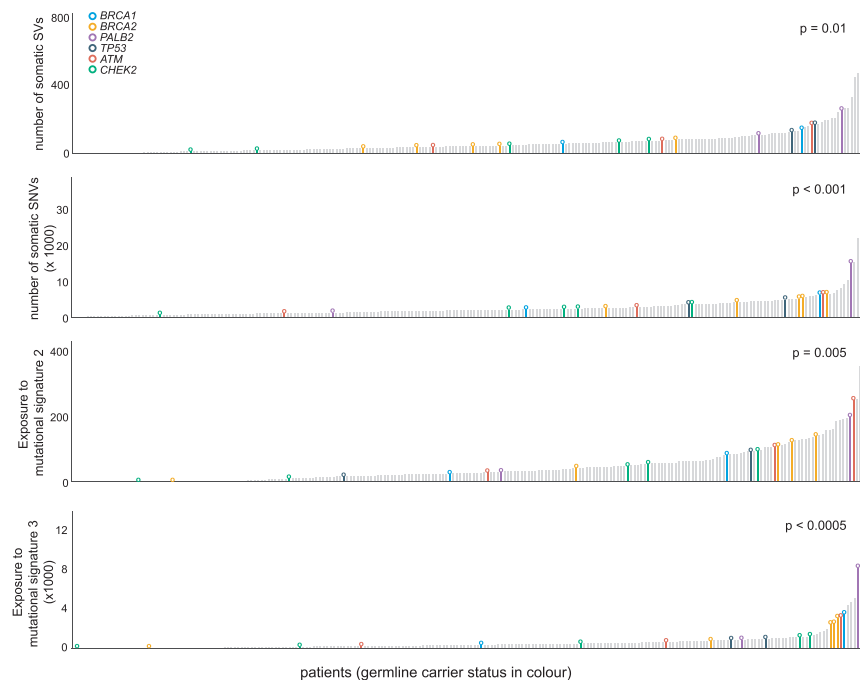


Figure 4. Predisposing Germline Mutations Associate with Specific Somatic Alteration Landscapes

Association between individuals carrying germline PTV in the indicated cancer predisposition gene and total number of somatic SVs, total number of somatic SNVs, exposure to mutational signature 2 and mutational signature 3. The x axis represents patients, sorted in ascending order of the phenotype. MWU-based p values.

integrated CC expression profiles, ct content, and PEPCI information to further refine the PEPCI-based risk stratification (Figures 6A–6C, see the [STAR Methods](#)). This led us to identify a prominent PC subgroup 1 of mainly PEPCI-high tumors (19 samples) with high content of T-luminal cells and expression of CC7 (Figures 6B and 6C). CC7 is associated with reactive stroma, which is indicated by an enriched myofibroblast signature and the reactive stroma marker ASPN in CC7 (Barron and Rowley, 2012; Rochette et al., 2017). Subgroup 1 was also associated with prominent loss of CC2 and CC4 gene expression representing normal basal and luminal prostate epithelium (Strand and Goldstein, 2015). CC2 loss and CC7 gain were strongly and independently linked to GS (Figure S5B) and BCR (Figure 6D). Multivariable statistics showed that CC2 adds significant information on top of GS in predicting BCR in both our cohort and in the TCGA cohort ($p = 0.003$ and $p = 0.01$, respectively; Table S4). In addition, CC2-low and CC7-high tumors were associated with specific RGAs, in particular *PTEN* loss ($p < 0.0001$, both) and *ESRP1* gain ($p < 0.0001$ and $p < 0.0005$, respectively, Pearson's chi-square test).

A small group of PEPCI-high tumors, termed PC subgroup 2, was associated with high CC1 (immune), CC5 (stroma), and CC7 (reactive stroma) expression and very high immune cell content, but low T-luminal cell content (Figures 6B and 6C). Consistent with the CC2-low and/or CC7-high expression profiles, subgroups 1 and 2 were strongly associated with high GS (Figure 6E) and shorter time to BCR (Figure 6F).

PC subgroup 3 was associated with high CC5 (stroma) and represented an intermediate-risk group. The last subgroup, termed PC subgroup 4, was PEPCI-low and associated with a high fraction of normal-like luminal cells, CC2 and CC4 (basal/epithelial) expression and a known gene signature associated with less-aggressive PC (Jhun et al., 2017) (Figure 6F). We observed an enrichment for a *TMPRSS2-ERG*-related gene

signature in CC3 (Figure 6A) and a significant enrichment for ETS fusions in CC3-high tumors ($p < 1 \times 10^{-13}$, Mann-Whitney U test; Figure S5A). CC3 did not associate strongly with any of the four subgroups.

We validated the CCs and clinical relevance of the subgroups in the TCGA cohort of 462 PC samples with available RNA-seq data (Figure S6A–S6E). The subgroups showed an improved prediction of BCR compared with GS alone in GS7 cases of the TCGA cohort ($p = 0.015$; Table S4). Importantly, most PEPCI-high

GS7 cases in the TCGA cohort belonged to subgroup 3 (Figures S6F–S6H), supporting our hypothesis of an intermediate-risk group. Comparing subgroups between the two age-of-onset groups identified a higher occurrence of subgroup 4 in EOPC (associated with better prognosis) ($p = 0.008$, adjusted for GS, Table S4), suggesting age-associated differences in the subgroups. In summary, our integrated analysis of CC signatures and PEPCI score stratified the patients into four prognostic relevant subgroups with distinct differences in the expression of biological pathways.

Tracing the Temporal Order and Clinical Trajectories of PC

Defining the temporal order of somatic events during tumorigenesis can give fundamental insights into the mutational process, clinical trajectories, and ultimately guide therapeutic decision making. Prior work has utilized various methods including linear models, tree-based models, clustering, or Bayesian approaches to delineate the most likely sequences of somatic events (Lecca et al., 2015; Ramazzotti et al., 2015). A particular relevant question that was not previously addressed is to identify both the most likely next molecular event at any given point and the associated clinical outcome, conditioned on the occurrence of all preceding mutations in that tumor. Our EOPC cohort provides an attractive sample set to address this, due to enrichment of the earliest somatic events and higher clonality (Figure S7A). To identify the temporal order of events in our cohort, we developed PRESCIENT (prediction of sequential changes in the evolution of nascent tumors), a conditional probability-based network model to predict the temporal sequence of somatic events in PC and associated clinical outcome. PRESCIENT uses the probability of observing two events as the exclusive events in the tumor (formulated as exclusion score [E]), with high E as a proxy for early, clonal events. *ERG* had the single highest E value

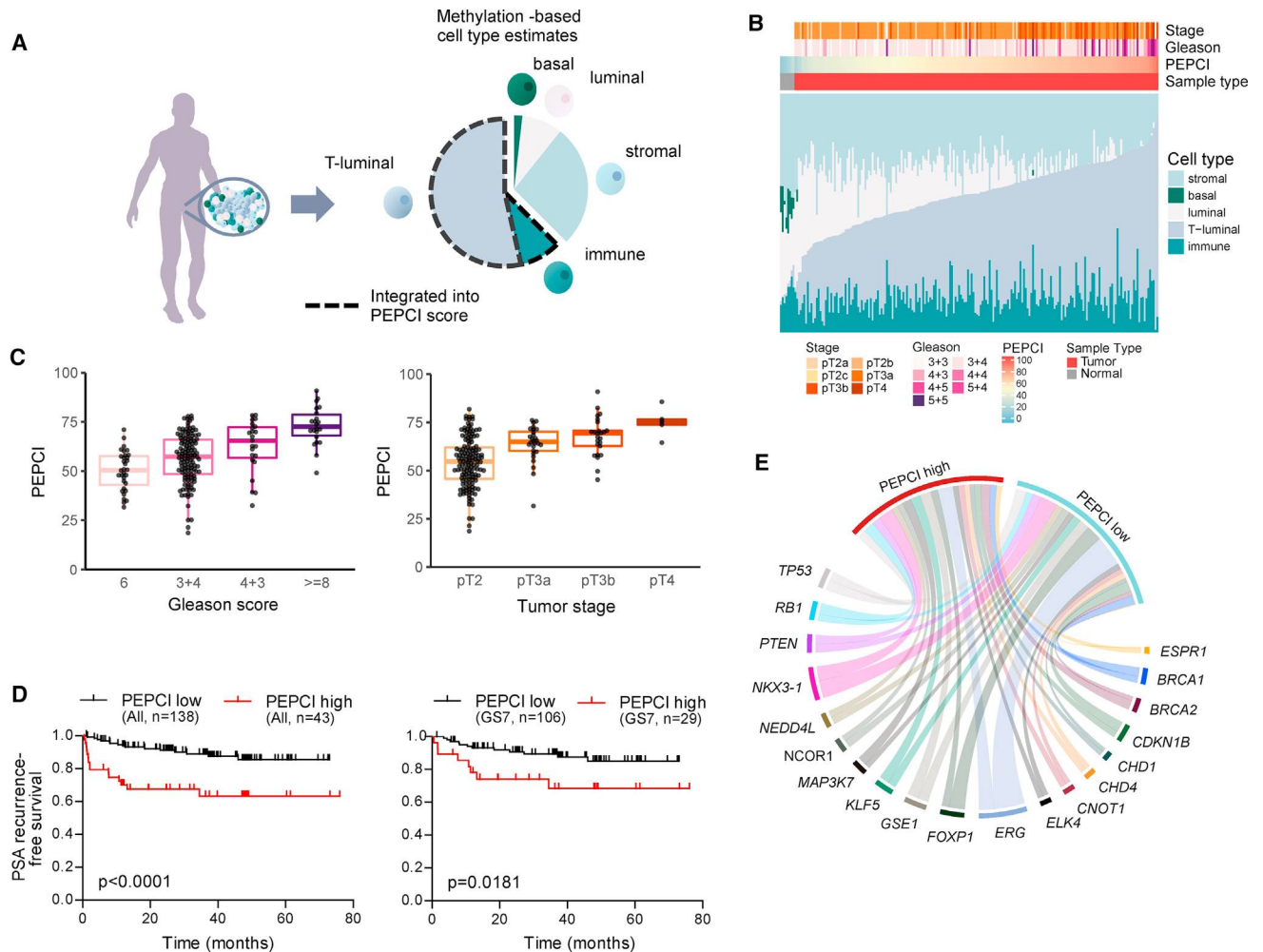


Figure 5. PEPCI, a Methylation-Based Risk Group Score

(A) A schematic representation of methylation-based estimation of ct composition of each bulk tumor sample.

(B) Stacked barplots of ct composition, tumor stage, GS and PEPCI per PC.

(C) Association between PEPCI and GS (left) and pT (right). Boxplots show median (line), upper and lower quartiles (boxes), and lines extending to 1.5 × IQR (whiskers).

(D) Kaplan-Meier curves of localized EOPC patients stratified according to PEPCI-high and PEPCI-low, for all cases (left) and for GS7 only (right). Log-rank test.

(E) Chord diagram showing proportions of tumors with a specific RGA and the associated PEPCI-high- and low-risk group, colored by each RGA.

See also [Figure S4](#) and [Table S3](#).

($E_{ERG,ERG}$, diagonal on [Figure 7A](#)), followed by *ERG* together with *FOXP1* ($E_{ERG,FOXP1}$), with both RGAs having a high level of connections to other RGAs ([Figure S7B](#)), suggesting that *ERG* is frequently occurring as the initial event, followed by *FOXP1*. A pathway-level analysis showed paths including an initiating ETS fusion event followed by events involved in AR-signaling or cell cycle and subsequent pathway-level events ([Figure 7B](#)).

For every node in the network, PRESCIENT uses molecular markers to predict the associated probability of event-free survival (PEFS) ([Figures 7A](#), [S7B](#), and [S7C](#)). We verified the ability of PRESCIENT to infer the order of mutational events by performing random subsampling and by cross-validation through WGS and reconstruction of the molecular evolution from 40 PC patients developing local metastases. Cross-validation showed robust sensitivity and specificity for PRESCIENT ([Figure S7D](#)),

providing support that with a given patient's tumor being molecularly profiled, our probabilistic model is able to predict a patient's next mutational event more accurately than frequency-based estimates.

We next sought to test our ability to predict aggressiveness of clones from a tumor phylogeny by performing multi-regional WGS of seven EOPC genomes ([Figure 7C](#)), followed by clonal reconstruction. For every tumor clone in the tree, we applied our conditional probability model to predict the PEFS (color-scale in [Figure 7B](#)). For tumors with divergence in aggressiveness of subclones, i.e., for branches with differences in PEFS, the branch with the shorter PEFS was also the more dominant clone, that is, the tumor clone with the highest relative contribution to the tumor mass from the sampled areas (see, e.g., PCA036 in [Figure 7C](#) and PCA037 in [Figure S7E](#)). This suggested

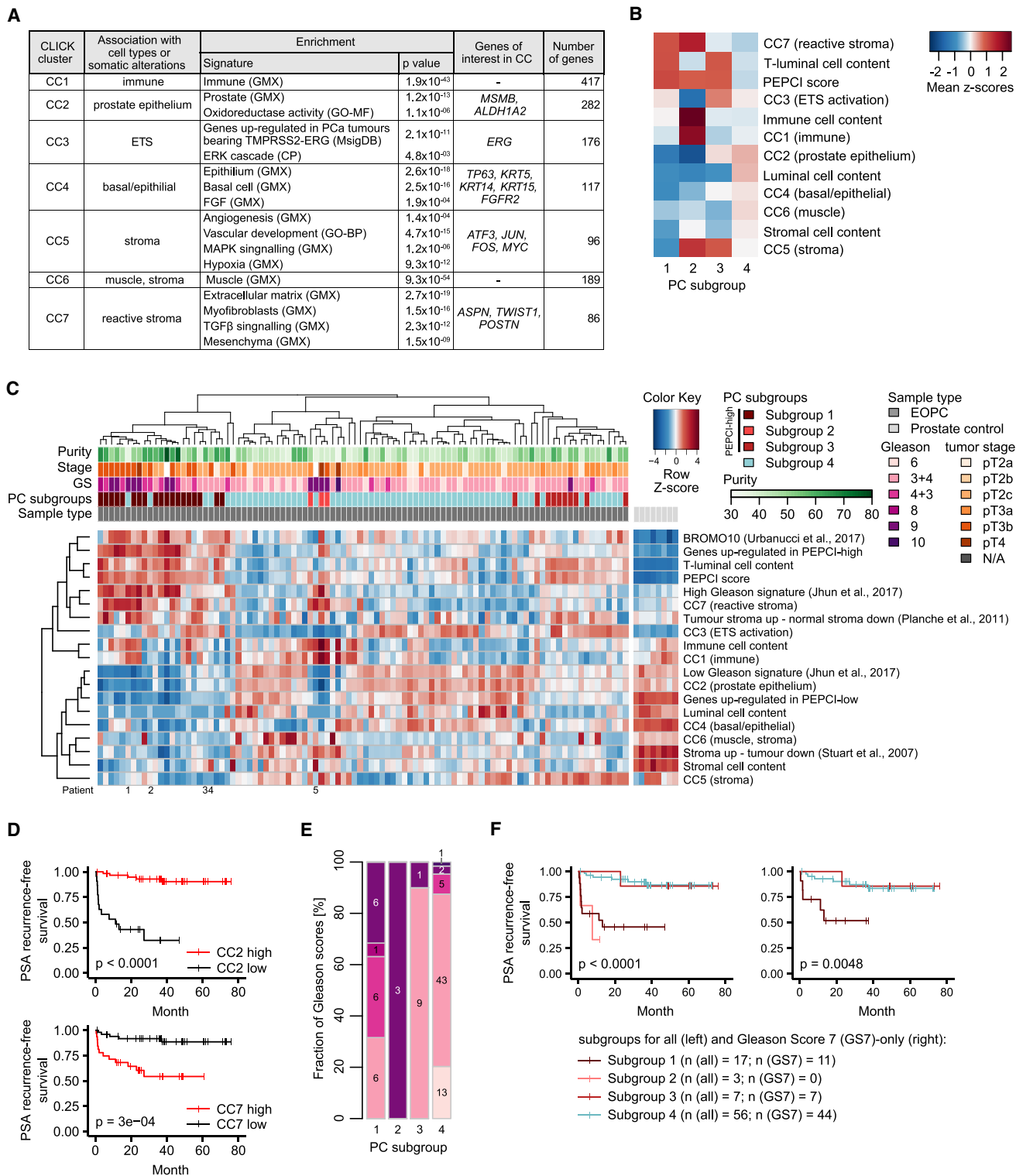


Figure 6. Integrative Expression and Methylation Analysis

(A) Summary of the most prominent characteristics of CCs. Sources of gene sets are indicated in the brackets: GMX, Genomatrix-curated gene sets; GO-MF and GO-BF, molecular and biological functions in gene ontology terms, respectively; CP, Genomatrix canonical pathways. False discovery rate-corrected $p < 0.05$.

(B) Heatmap of the four PC subgroups and their average ct compositions and CC mean pattern values.

(C) Hierarchical clustering heatmap of ct content, CCs, three external gene signatures and indicated PC subgroups across 96 EOPC samples and eight normal prostate controls. CCs and external gene signatures are represented as mean pattern values. Clustering was based on PEPCI-related features and CC (legend continued on next page)

that genomic profiling of several areas of a tumor can be used to identify the more dominant, aggressive clone and pointed toward the utility of applying a probabilistic modeling in order to predict aggressiveness.

PCA041 displayed a particular aggressive molecular evolution involving an early, clonal *ESRP1* gain. Both branches maintained an aggressive phenotype, with one branch acquiring *KLF5*, *BRCA1*, and *RB1* loss and another branch acquiring two parallel biallelic inactivation events of *PTEN* and *TP53* (Figure 7C).

We tested the ability to predict the disease course based on a single biopsy using PRESCIENT. As a first approximation, we used single-sampled areas from PCA035 to predict both PEFS and the next molecular alteration (Figure 7D). We note that the phylogenetic trees were based on a Bayesian mixture model that uses information from all individual sequenced areas of one tumor and a single sample could therefore in most cases not uniquely be assigned to one branch. We found that the PEFS predicted from a single area of the tumor tended to initiate differently but eventually converged, as exemplified for tumor area T5 (Figure 7D), suggesting that the initiating RGAs in T5 were sufficient to predict the clinical trajectory of the tumor.

Finally, we assessed the potential to identify targeted therapies (Tamborero et al., 2018) based on germline and somatic genomic data. More than 40% of the EOPC patients could be matched with at least one targeted therapy in either pre-clinical test or clinical trial for PC. The targeted agents included phosphatidylinositol 3-kinase, mammalian target of rapamycin, and poly (ADP-ribose) polymerase (PARP) inhibitors (Figure S7F), with the majority of *BRCA2*-mutated patients showing high levels of somatic BRCAness mutation signature 3 and a high mutational burden (see also Figures 3 and 4), suggesting that these patients could benefit from PARP inhibitors.

In summary, taking advantage of our EOPC cohort, we developed a statistical framework that uses molecular markers to predict the most likely next somatic alteration and associated change in event-free survival.

DISCUSSION

Deciphering the molecular evolution and clinical trajectories of PC require a comprehensive and integrative analysis of the early molecular alterations and mutational mechanisms. A previous survey identified age-associated mutations as the most common mutational process in cancer followed by APOBEC mutagenesis (Alexandrov et al., 2013; Roberts and Gordenin, 2014). Our analysis revealed that APOBEC-associated mutations and kataegis clusters show a clock-like behavior in PC. This mutational process, in PC, is primarily attributable to APOBEC3B activity, likely due to a residual albeit constant enzymatic activity.

Our data suggest that APOBEC-attributable mutations occur throughout the development of PC as well as in the normal prostate tissue prior to transformation. Thus, APOBEC mutagenesis and the resulting kataegis events, some of which occur in conjunction with SV formation, are likely to contribute to the earliest mutations seen in PC.

Whereas mutational signatures bear trace of the age and exposure of the tissue, somatic SVs frequently cause tumor-promoting gene dysregulation. We identified recurrent breakpoint hotspots including a potentially clinically relevant biomarker at 8q22, associated with genomic duplication of *ESRP1*. *ESRP1* has been demonstrated to take part in RAF fusion formation in PC (Palanisamy et al., 2010), although we did not find evidence for *ESRP1* fusion events in our cohort. *ESRP1* has also been implicated in EMT transition (Ishii et al., 2014) and overexpression has been demonstrated to cause anchorage-independent growth and metastases in colorectal cancer (Fagoonee et al., 2017). *ESRP1* was previously shown to be strongly co-expressed with E-cadherin, and increased expression of *ESRP1* may therefore lead to accelerated proliferation of an epithelial cell state.

PC is a highly heterogeneous disease, but there is a limited understanding of the ct composition and how this impacts disease progression. Recent genomic surveys have characterized seven subtypes based on somatic alterations (TCGA, 2015), primarily involving ETS family genes, but the ct composition and associated clinical relevance remained unexplored. Analysis of basal and luminal ct composition has shown biological and clinical relevance in another hormone-associated adenocarcinoma—breast cancer (Sotiriou et al., 2003). We pursued a complementary approach by integrating methylation array and RNA-seq data, which led us to identify four molecular subgroups based on ct composition and gene expression patterns in EOPC tumors that showed association with clinical outcome independent of GS. The subgroups were able to stratify intermediate-risk GS7 PC cases, suggesting that the subgroup information can serve as an independent molecular risk score. Tumors that differ in ct composition would likely respond differentially to therapies, and further work will be needed to investigate whether the different subgroups predict response to therapy.

There is an urgent need for biomarkers that can stratify patients who need definitive treatment from those who can follow active surveillance or watchful waiting. Single biomarkers are unlikely to be useful in a heterogeneous and complex disease such as PC, and multiple biomarkers will thus be required to guide clinical decision making. We utilized our comprehensive molecular catalog of the earliest alterations in PC to develop PRESCIENT. PRESCIENT establishes a knowledge-based framework for future genomics-informed patient stratification and drug targeting. The current implementation is limited

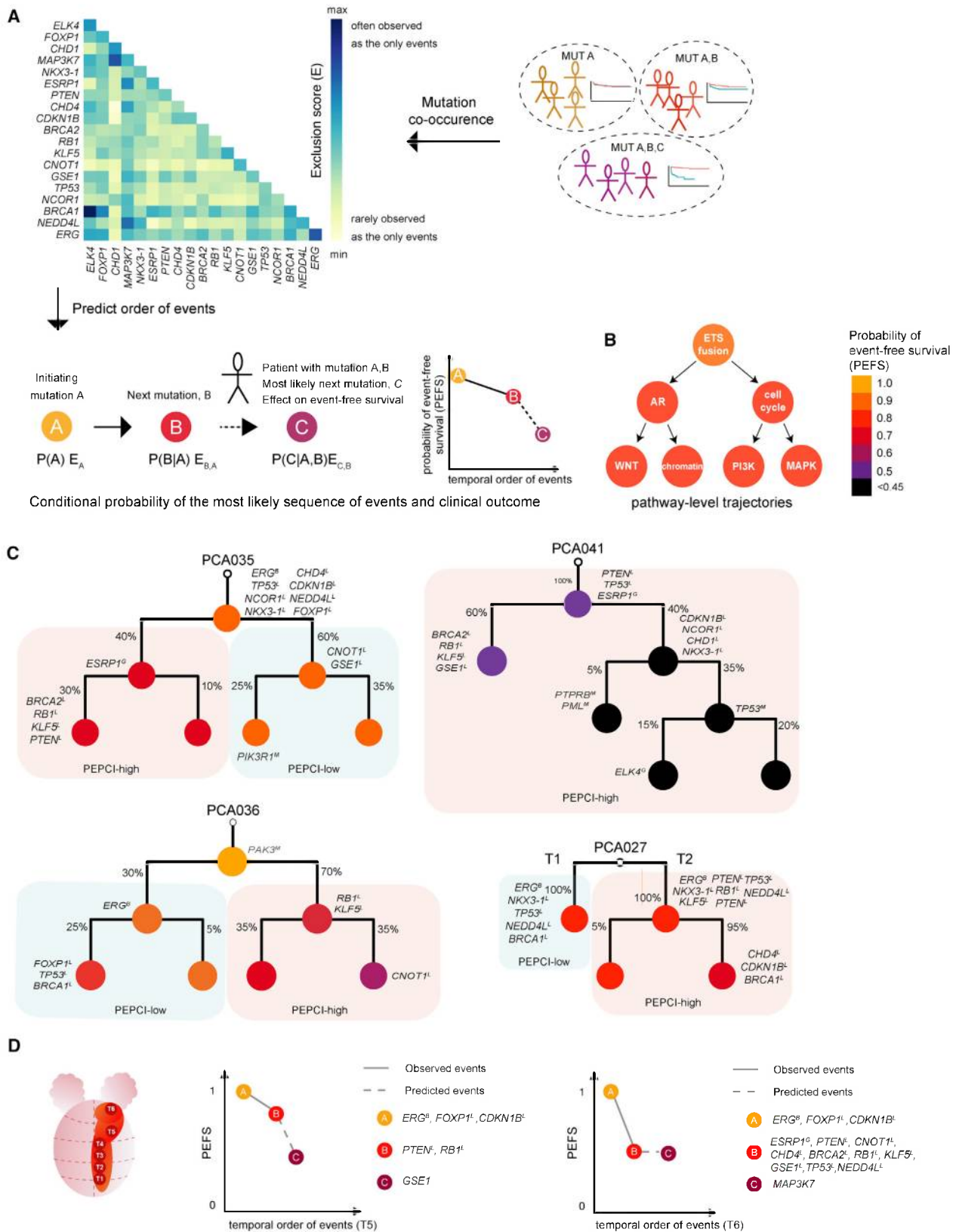
information (excluding CC6 due to low information content). Patient numbers 1 and 3: PEPCI score just below the Inflection point, no. 2 multi-area sample with varying PEPCI score, no. 4 and no. 5 high stromal content.

(D) Kaplan-Meier curves between subgroups in CC2 and CC7 and event-free survival (log rank test).

(E) Stacked barplot of fraction of GS in the four PC subgroups.

(F) Kaplan-Meier curves of the four PC subgroups using ICGC EOPC samples with available methylation and RNA-seq data (left, $n = 83$) and a subset of GS7 cases (right, $n = 62$). Log-rank test.

See also Table S4 and Figures S5 and S6.



(legend on next page)

in the sample cohort size, which we expect to improve in both sensitivity and specificity with inclusion of more samples. This will involve highly aggressive tumors, including LOPC and metastatic cancers, to increase the ability to predict event-free survival and therapy response, as well as enable the prediction of secondary alterations associated with metastasis.

STAR METHODS

Detailed methods are provided in the online version of this paper and include the following:

- **KEY RESOURCES TABLE**
- **CONTACT FOR REAGENT AND RESOURCE SHARING**
- **EXPERIMENTAL MODEL AND SUBJECT DETAILS**
 - Human Subjects
 - Tissue-Microarray Processing
- **METHOD DETAILS**
 - Biospecimens and Quality Control
 - Nucleic Acid Sequencing and Analysis
 - Read Alignment
 - Median Purity
 - Single-Nucleotide Variant and SV Calling
 - Subclonal Copy-Number Analysis
- **QUANTIFICATION AND STATISTICAL ANALYSIS**
- **DATA AND SOFTWARE AVAILABILITY**

ACKNOWLEDGMENTS

We thank the patients and families who contributed to this study. The study was funded by the ICGC EOPC (01KU1001 A) and ICGC-Data Mining (01KU1505A) projects on early-onset prostate cancer by the German Federal Ministry of Education and Research (BMBF). The authors acknowledge the DKFZ, MPI and EMBL Genomics Core Facilities. J.W., F.F., and N. Sidiropoulos were supported by Arvid Nilsson Foundation and Rigshospitalets forskningsfond. R.S. and R.T. were supported by Sander Stiftung (no. 2015.010.1). J.O.K. was, in part, supported by an ERC Starting Grant. C.F. received a stipend by the Helmholtz International Graduate School at the DKFZ. A.U. is supported by the Research Council of Norway (no. 187615). D.A.G. was supported by the US NIH Intramural Research Program Project Z1AES103266.

AUTHOR CONTRIBUTIONS

J.W. wrote the original draft with contributions from T.R. and C.G.; Writing — Review & Editing, J.W., C.G., F.F., T.R., T.S., J.O.K., M.-L.Y., C.P., G.S., S.M.W., P.C.B., B.B., H.S., C.v.K., L.F., D.W., D. Hubschmann, and Y.A.; Conceptualization, J.W., T.S., M.-L.Y., J.O.K., L.F., and B.B.; Supervision, J.W., T.S., J.O.K., M.-L.Y., C.P., G.S., B.B., L.F., H.S., and D.G.; Study Design,

T.S., J.O.K., G.S., J.W., and M.-L.Y.; Funding Acquisition, T.S., J.O.K., C.P., G.S., B.B., H.S., C.v.K., M.-L.Y., J.W., and L.F.; Sample Providers, G.S., T.S., M.G., H.H., R.G.B., P.C.B., T.N.Y., and D.S.; Formal Analysis, J.W., T.R., F.F., C.G., R.S., S.M.W., N. Sidiropoulos, D.G., Y.A., J.O.K., D.S., A.M., G.H.H., V.A., H.-J.W., S.M., P.L., J.D.H., O.B., R.T., L.J.K., E.G.G., V.K., A.U., D. Heckmann, L.F., N.S.I., and D. Hubschmann; Visualization, J.W., F.F., T.R., C.G., N. Sidiropoulos, Y.A., R.S., S.M.W., N. Saini, and L.F.; Resources, M.-L.Y., D.W.S., E.R., C.L., A.U., R.S., R.T., B.B., and R.E.; Validation, J.M., M.K., C.H., C.K., L.-M.B., D.W., and R.S.; Software, F.F., Y.A., T.R., C.G., N. Sidiropoulos, J.W., E.R., C.L., C.F., V.A., H.-J.W., S.M., P.L., L.F., V.K., and D. Hubschmann; Data Curation, L.F., Y.A., V.K., C.L., and E.R.; Methodology, F.F., T.R., C.G., J.W., N. Sidiropoulos, J.M., M.K., C.H., C.K., E.G.G., R.T., D.W., A.M.S., D. Hubschmann, and B.R.

DECLARATION OF INTERESTS

The authors declare no competing interests.

REFERENCES

- Alexandrov, L.B., Nik-Zainal, S., Wedge, D.C., Aparicio, S.A., Behjati, S., Biankin, A.V., Bignell, G.R., Bolli, N., Borg, A., Borresen-Dale, A.L., et al. (2013). Signatures of mutational processes in human cancer. *Nature* 500, 415–421.
- 1000 Genomes Project Consortium, Auton, A., Brooks, L.D., Durbin, R.M., Garrison, E.P., Kang, H.M., Korbel, J.O., Marchini, J.L., McCarthy, S., McVean, G.A., et al. (2015). A global reference for human genetic variation. *Nature* 526, 68–74.
- Alexandrov, L.B., Jones, P.H., Wedge, D.C., Sale, J.E., Campbell, P.J., Nik-Zainal, S., and Stratton, M.R. (2015). Clock-like mutational processes in human somatic cells. *Nat. Genet.* 47, 1402–1407.
- Aran, D., Sirota, M., and Butte, A.J. (2015). Systematic pan-cancer analysis of tumour purity. *Nat. Commun.* 6, 8971.
- Aryee, M.J., Liu, W., Engelmann, J.C., Nuhn, P., Gurel, M., Haffner, M.C., Esopi, D., Irizarry, R.A., Getzenberg, R.H., Nelson, W.G., et al. (2013). DNA methylation alterations exhibit intraindividual stability and interindividual heterogeneity in prostate cancer metastases. *Sci. Transl. Med.* 5, 169ra10.
- Asangani, I.A., Dommeti, V.L., Wang, X., Malik, R., Cieslik, M., Yang, R., Escara-Wilke, J., Wilder-Romans, K., Dhanireddy, S., Engelke, C., et al. (2014). Therapeutic targeting of BET bromodomain proteins in castration-resistant prostate cancer. *Nature* 510, 278–282.
- Assenov, Y., Müller, F., Lutsik, P., Walter, J., Lengauer, T., and Bock, C. (2014). Comprehensive analysis of DNA methylation data with RnBeads. *Nat. Methods* 11, 1138–1140.
- Barfeld, S.J., Urbanucci, A., Itkonen, H.M., Fazli, L., Hicks, J.L., Thiede, B., Rennie, P.S., Yegnasubramanian, S., DeMarzo, A.M., and Mills, I.G. (2017). c-Myc antagonises the transcriptional activity of the androgen receptor in prostate cancer affecting key gene networks. *EBioMedicine* 18, 83–93.
- Barron, D.A., and Rowley, D.R. (2012). The reactive stroma microenvironment and prostate cancer progression. *Endocr. Relat. Cancer* 19, R187–R204.

Figure 7. Molecular Evolution of PC

- (A) Outline of the PRESCIENT method.
- (B) RGAs were labeled with a molecular pathway, which was used as an event in PRESCIENT.
- (C) Molecular reconstruction of individual EOPC tumors, using a Bayesian mixture model with each node annotated with RGAs and event-free survival prediction (color range). The clonal status is annotated with percentages at each branch. Mutations in COSMIC genes are annotated in gray for each node. Branches are labeled by background color based on PEPCI score for PEPCI-high and PEPCI-low.
- (D) A schematic representation of PCA035 (left) and application of PRESCIENT prediction to T5 (middle) and T6 (right) regions of the tumor.
- See also Figure S7.

- Bhasin, J.M., Lee, B.H., Matkin, L., Taylor, M.G., Hu, B., Xu, Y., Magi-Galluzzi, C., Klein, E.A., and Ting, A.H. (2015). Methylome-wide sequencing detects DNA hypermethylation distinguishing indolent from aggressive prostate cancer. *Cell Rep.* 13, 2135–2146.
- BLUEPRINT consortium (2016). Quantitative comparison of DNA methylation assays for biomarker development and clinical applications. *Nat. Biotechnol.* 34, 726–737.
- Börn, S.T., Fischer, A., Kerick, M., Fälth, M., Laible, M., Brase, J.C., Kuner, R., Dahl, A., Grimm, C., Sayanali, B., et al. (2012). Genome-wide DNA methylation events in TMPRSS2-ERG fusion-negative prostate cancers implicate an EZH2-dependent mechanism with miR-26a hypermethylation. *Cancer Discov.* 2, 1024–1035.
- Boutros, P.C., Fraser, M., Harding, N.J., de Borja, R., Trudel, D., Lalonde, E., Meng, A., Hennings-Yeomans, P.H., McPherson, A., Sabelnykova, V.Y., et al. (2015). Spatial genomic heterogeneity within localized, multifocal prostate cancer. *Nat. Genet.* 47, 736–745.
- Brocks, D., Assenov, Y., Minner, S., Bogatyrova, O., Simon, R., Koop, C., Oakes, C., Zucknick, M., Lipka, D.B., Weischenfeldt, J., et al. (2014). Intratumor DNA methylation heterogeneity reflects clonal evolution in aggressive prostate cancer. *Cell Rep.* 8, 798–806.
- Carter, S.L., Cibulskis, K., Helman, E., McKenna, A., Shen, H., Zack, T., Laird, P.W., Onofrio, R.C., Winckler, W., Weir, B.A., et al. (2012). Absolute quantification of somatic DNA alterations in human cancer. *Nat. Biotechnol.* 30, 413–421.
- Chae, M., Danko, C.G., and Kraus, W.L. (2015). groHMM: a computational tool for identifying unannotated and cell type-specific transcription units from global run-on sequencing data. *BMC Bioinformatics* 16, 222.
- Chan, K., and Gordenin, D.A. (2015). Clusters of multiple mutations: incidence and molecular mechanisms. *Annu. Rev. Genet.* 49, 243–267.
- Chan, K., Roberts, S.A., Klimczak, L.J., Sterling, J.F., Saini, N., Malc, E.P., Kim, J., Kwiatkowski, D.J., Fargo, D.C., Mieczkowski, P.A., et al. (2015). An APOBEC3A hypermutation signature is distinguishable from the signature of background mutagenesis by APOBEC3B in human cancers. *Nat. Genet.* 47, 1067–1072.
- Chen, Y., Chi, P., Rockowitz, S., laquinta, P.J., Shamu, T., Shukla, S., Gao, D., Sirota, I., Carver, B.S., Wongvipat, J., et al. (2013a). ETS factors reprogram the androgen receptor cistrome and prime prostate tumorigenesis in response to PTEN loss. *Nat. Med.* 19, 1023–1029.
- Chen, Y.-A., Lemire, M., Choufani, S., Butcher, D.T., Grafodatskaya, D., Zanke, B.W., Gallinger, S., Hudson, T.J., and Weksberg, R. (2013b). Discovery of cross-reactive probes and polymorphic CpGs in the Illumina Infinium HumanMethylation450 microarray. *Epigenetics* 8, 203–209.
- Chen, H., Li, C., Peng, X., Zhou, Z., Weinstein, J.N.; Cancer Genome Atlas Research Network, and Liang, H. (2018). A pan-cancer analysis of enhancer expression in nearly 9000 patient samples. *Cell* 173, 386–399.e12.
- Desper, R., and Gascuel, O. (2002). Fast and accurate phylogeny reconstruction algorithms based on the minimum-evolution principle. *J. Comput. Biol.* 9, 687–705.
- Durand, N.C., Shamim, M.S., Machol, I., Rao, S.S.P., Huntley, M.H., Lander, E.S., and Aiden, E.L. (2016). Juicer provides a one-click system for analyzing loop-resolution Hi-C experiments. *Cell Syst.* 3, 95–98.
- Erbersdobler, A., Hammerer, P., Huland, H., and Henke, R.P. (1997). Numerical chromosomal aberrations in transition-zone carcinomas of the prostate. *J. Urol.* 158, 1594–1598.
- Ernst, J., and Kellis, M. (2012). ChromHMM: automating chromatin-state discovery and characterization. *Nat. Methods* 9, 215–216.
- Espirito, S.M.G., Liu, L.Y., Rubanova, Y., Bhandari, V., Holgersen, E.M., Szyca, L.M., Fox, N.S., Chua, M.L.K., Yamaguchi, T.N., Heisler, L.E., et al. (2018). The evolutionary landscape of localized prostate cancers drives clinical aggression. *Cell* 173, 1003–1013.e15.
- Fagoonee, S., Picco, G., Orso, F., Arrigoni, A., Longo, D.L., Forni, M., Scarfò, I., Cassenti, A., Piva, R., Cassoni, P., et al. (2017). The RNA-binding protein ESRP1 promotes human colorectal cancer progression. *Oncotarget* 8, 10007–10024.
- Favero, F., Joshi, T., Marquard, A.M., Birkbak, N.J., Krzystanek, M., Li, Q., Szallasi, Z., and Eklund, A.C. (2015). Sequenza: allele-specific copy number and mutation profiles from tumor sequencing data. *Ann. Oncol.* 26, 64–70.
- Fraser, M., Sabelnykova, V.Y., Yamaguchi, T.N., Heisler, L.E., Livingstone, J., Huang, V., Shiah, Y.-J., Yousif, F., Lin, X., Masella, A.P., et al. (2017). Genomic hallmarks of localized, non-indolent prostate cancer. *Nature* 541, 359–364.
- Henry, G.H., Loof, N., and Strand, D.W. (2017). OMIP-040: optimized gating of human prostate cellular subpopulations. *Cytometry A* 91, 1147–1149.
- Hnisz, D., Abraham, B.J., Lee, T.I., Lau, A., Saint-André, V., Sigova, A.A., Hoke, H.A., and Young, R.A. (2013). Super-enhancers in the control of cell identity and disease. *Cell* 155, 934–947.
- Houseman, E.A., Accomando, W.P., Koestler, D.C., Christensen, B.C., Marsit, C.J., Nelson, H.H., Wiencke, J.K., and Kelsey, K.T. (2012). DNA methylation arrays as surrogate measures of cell mixture distribution. *BMC Bioinformatics* 13, 86.
- Huebschmann, D., Gu, Z., and Schlesner, M. (2016). YAPSA: yet another package for signature analysis. R Package Version 0.99.10. <https://doi.org/10.18129/B9.bioc.YAPSA>.
- Ishii, H., Saitoh, M., Sakamoto, K., Kondo, T., Katoh, R., Tanaka, S., Motizuki, M., Masuyama, K., and Miyazawa, K. (2014). Epithelial splicing regulatory proteins 1 (ESRP1) and 2 (ESRP2) suppress cancer cell motility via different mechanisms. *J. Biol. Chem.* 289, 27386–27399.
- Ishwaran, H., Kogalur, U.B., Blackstone, E.H., and Lauer, M.S. (2008). Random survival forests. *Ann. Appl. Stat.* 2, 841–860.
- Jeong, H.M., Han, J., Lee, S.H., Park, H.-J., Lee, H.J., Choi, J.-S., Lee, Y.M., Choi, Y.-L., Shin, Y.K., and Kwon, M.J. (2017). ESRP1 is overexpressed in ovarian cancer and promotes switching from mesenchymal to epithelial phenotype in ovarian cancer cells. *Oncogenesis* 6, e389.
- Jhun, M.A., Geybels, M.S., Wright, J.L., Kolb, S., April, C., Bibikova, M., Ostrander, E.A., Fan, J.-B., Feng, Z., and Stanford, J.L. (2017). Gene expression signature of Gleason score is associated with prostate cancer outcomes in a radical prostatectomy cohort. *Oncotarget* 8, 43035–43047.
- Jiang, Y., Qiu, Y., Minn, A.J., and Zhang, N.R. (2016). Assessing intratumor heterogeneity and tracking longitudinal and spatial clonal evolutionary history by next-generation sequencing. *Proc. Natl. Acad. Sci. U S A* 113, E5528–E5537.
- Kluth, M., Hesse, J., Heini, A., Krohn, A., Steurer, S., Sirma, H., Simon, R., Mayer, P.-S., Schumacher, U., Grupp, K., et al. (2013). Genomic deletion of MAP3K7 at 6q12-22 is associated with early PSA recurrence in prostate cancer and absence of TMPRSS2:ERG fusions. *Mod. Pathol.* 26, 975–983.
- Kononen, J., Bubendorf, L., Kallioniemi, A., Bärnlund, M., Schraml, P., Leighton, S., Torhorst, J., Mihatsch, M.J., Sauter, G., and Kallioniemi, O.P. (1998). Tissue microarrays for high-throughput molecular profiling of tumor specimens. *Nat. Med.* 4, 844–847.
- Kron, K.J., Murison, A., Zhou, S., Huang, V., Yamaguchi, T.N., Shiah, Y.-J., Fraser, M., van der Kwast, T., Boutros, P.C., Bristow, R.G., et al. (2017). TMPRSS2-ERG fusion co-opts master transcription factors and activates NOTCH signaling in primary prostate cancer. *Nat. Genet.* 49, 1336–1345.
- Lecca, P., Casiraghi, N., and Demicheli, F. (2015). Defining order and timing of mutations during cancer progression: the TO-DAG probabilistic graphical model. *Front. Genet.* 6, 309.
- Li, H. (2013). Aligning sequence reads, clone sequences and assembly contigs with BWA-MEM. *arXiv* 1303.3997v2.
- Locke, J.A., Zafarana, G., Ishkanian, A.S., Milosevic, M., Thoms, J., Have, C.L., Malloff, C.A., Lam, W.L., Squire, J.A., Pintilie, M., et al. (2012). NKX3.1 haploinsufficiency is prognostic for prostate cancer relapse following surgery or image-guided radiotherapy. *Clin. Cancer Res.* 18, 308–316.
- Massie, C.E., Lynch, A., Ramos-Montoya, A., Boren, J., Stark, R., Fazli, L., Warren, A., Scott, H., Madhu, B., Sharma, N., et al. (2011). The androgen receptor fuels prostate cancer by regulating central metabolism and biosynthesis. *EMBO J.* 30, 2719–2733.

- Middlebrooks, C.D., Banday, A.R., Matsuda, K., Udquim, K.-I., Onabajo, O.O., Paquin, A., Figueroa, J.D., Zhu, B., Koutros, S., Kubo, M., et al. (2016). Association of germline variants in the APOBEC3 region with cancer risk and enrichment with APOBEC-signature mutations in tumors. *Nat. Genet.* **48**, 1330–1338.
- Mortazavi, A., Williams, B.A., McCue, K., Schaeffer, L., and Wold, B. (2008). Mapping and quantifying mammalian transcriptomes by RNA-Seq. *Nat. Methods* **5**, 621–628.
- Myers, A., du Souich, C., Yang, C.L., Borovik, L., Mwenifumbo, J., Rupps, R., Study, C., Lehman, A., and Boerkoel, C.F. (2017). FOXP1 haploinsufficiency: phenotypes beyond behavior and intellectual disability? *Am. J. Med. Genet. A* **173**, 3172–3181.
- Na, R., Zheng, S.L., Han, M., Yu, H., Jiang, D., Shah, S., Ewing, C.M., Zhang, L., Novakovic, K., Petkewicz, J., et al. (2017). Germline mutations in ATM and BRCA1/2 distinguish risk for lethal and indolent prostate cancer and are associated with early age at death. *Eur. Urol.* **71**, 740–747.
- Nik-Zainal, S., Alexandrov, L.B., Wedge, D.C., Van Loo, P., Greenman, C.D., Raine, K., Jones, D., Hinton, J., Marshall, J., Stebbings, L.A., et al. (2012). Mutational processes molding the genomes of 21 breast cancers. *Cell* **149**, 979–993.
- Nik-Zainal, S., Davies, H., Staaf, J., Ramakrishna, M., Glodzik, D., Zou, X., Martincorena, I., Alexandrov, L.B., Martin, S., Wedge, D.C., et al. (2016). Landscape of somatic mutations in 560 breast cancer whole-genome sequences. *Nature* **534**, 47–54.
- Pageaud, Y., Plass, C., and Assenov, Y. (2018). Enrichment analysis with EpiAnnotator. *Bioinformatics* **34**, 1781–1783.
- Palanisamy, N., Ateeq, B., Kalyana-Sundaram, S., Pflueger, D., Ramnarayanan, K., Shankar, S., Han, B., Cao, Q., Cao, X., Suleman, K., et al. (2010). Rearrangements of the RAF kinase pathway in prostate cancer, gastric cancer and melanoma. *Nat. Med.* **16**, 793.
- Parisi, S., Cozzuto, L., Tarantino, C., Passaro, F., Ciriello, S., Aloia, L., Antonini, D., De Simone, V., Pastore, L., and Russo, T. (2010). Direct targets of Klf5 transcription factor contribute to the maintenance of mouse embryonic stem cell undifferentiated state. *BMC Biol.* **8**, 128.
- Planche, A., Bacac, M., Provero, P., Fusco, C., Delorenzi, M., Stehle, J.-C., and Stamenkovic, I. (2011). Identification of prognostic molecular features in the reactive stroma of human breast and prostate cancer. *PLoS One* **6**, e18640.
- Pound, C.R., Partin, A.W., Eisenberger, M.A., Chan, D.W., Pearson, J.D., and Walsh, P.C. (1999). Natural history of progression after PSA elevation following radical prostatectomy. *JAMA* **281**, 1591–1597.
- Pritchard, C.C., Mateo, J., Walsh, M.F., De Sarkar, N., Abida, W., Beltran, H., Garofalo, A., Gulati, R., Carreira, S., Eeles, R., et al. (2016). Inherited DNA-repair gene mutations in men with metastatic prostate cancer. *N. Engl. J. Med.* **375**, 443–453.
- Quinlan, A.R., and Hall, I.M. (2010). BEDTools: a flexible suite of utilities for comparing genomic features. *Bioinformatics* **26**, 841–842.
- Ramazzotti, D., Caravagna, G., Olde Loohuis, L., Graudenzi, A., Korsunsky, I., Mauri, G., Antonioti, M., and Mishra, B. (2015). CAPRI: efficient inference of cancer progression models from cross-sectional data. *Bioinformatics* **31**, 3016–3026.
- Rao, S.S.P., Huntley, M.H., Durand, N.C., Stamenova, E.K., Bochkov, I.D., Robinson, J.T., Sanborn, A.L., Machol, I., Omer, A.D., Lander, E.S., et al. (2014). A 3D map of the human genome at kilobase resolution reveals principles of chromatin looping. *Cell* **159**, 1665–1680.
- Rausch, T., Zichner, T., Schlatt, A., Stütz, A.M., Benes, V., and Korbel, J.O. (2012). DELLY: structural variant discovery by integrated paired-end and split-read analysis. *Bioinformatics* **28**, i333–i339.
- Roberts, S.A., and Gordenin, D.A. (2014). Hypermutation in human cancer genomes: footprints and mechanisms. *Nat. Rev. Cancer* **14**, 786–800.
- Roberts, S.A., Sterling, J., Thompson, C., Harris, S., Mav, D., Shah, R., Klimczak, L.J., Kryukov, G.V., Malc, E., Mieczkowski, P.A., et al. (2012). Clustered mutations in yeast and in human cancers can arise from damaged long single-strand DNA regions. *Mol. Cell* **46**, 424–435.
- Roberts, S.A., Lawrence, M.S., Klimczak, L.J., Grimm, S.A., Fargo, D., Stojanov, P., Kiezun, A., Kryukov, G.V., Carter, S.L., Saksena, G., et al. (2013). An APOBEC cytidine deaminase mutagenesis pattern is widespread in human cancers. *Nat. Genet.* **45**, 970–976.
- Robinson, M.D., and Oshlack, A. (2010). A scaling normalization method for differential expression analysis of RNA-seq data. *Genome Biol.* **11**, R25.
- Rochette, A., Boufaied, N., Scarlata, E., Hamel, L., Brimo, F., Whitaker, H.C., Ramos-Montoya, A., Neal, D.E., Dragomir, A., Aprikian, A., et al. (2017). Asporin is a stromally expressed marker associated with prostate cancer progression. *Br. J. Cancer* **116**, 775–784.
- Sharan, R., Maron-Katz, A., and Shamir, R. (2003). CLICK and EXPANDER: a system for clustering and visualizing gene expression data. *Bioinformatics* **19**, 1787–1799.
- Sotiriou, C., Neo, S.-Y., McShane, L.M., Korn, E.L., Long, P.M., Jazaeri, A., Martiat, P., Fox, S.B., Harris, A.L., and Liu, E.T. (2003). Breast cancer classification and prognosis based on gene expression profiles from a population-based study. *Proc. Natl. Acad. Sci. U S A* **100**, 10393–10398.
- Strand, D.W., and Goldstein, A.S. (2015). The many ways to make a luminal cell and a prostate cancer cell. *Endocr. Relat. Cancer* **22**, T187–T197.
- Stuart, R.O., Wachsman, W., Berry, C.C., Wang-Rodriguez, J., Wasserman, L., Klacansky, I., Masys, D., Arden, K., Goodison, S., McClelland, M., et al. (2004). In silico dissection of cell-type-associated patterns of gene expression in prostate cancer. *Proc. Natl. Acad. Sci. U S A* **101**, 615–620.
- Swanton, C., McGranahan, N., Starrett, G.J., and Harris, R.S. (2015). APOBEC enzymes: mutagenic fuel for cancer evolution and heterogeneity. *Cancer Discov.* **5**, 704–712.
- Taberlay, P.C., Statham, A.L., Kelly, T.K., Clark, S.J., and Jones, P.A. (2014). Reconfiguration of nucleosome-depleted regions at distal regulatory elements accompanies DNA methylation of enhancers and insulators in cancer. *Genome Res.* **24**, 1421–1432.
- Tamborero, D., Rubio-Perez, C., Deu-Pons, J., Schroeder, M.P., Vivancos, A., Rovira, A., Tusquets, I., Albanell, J., Rodon, J., Tabernero, J., et al. (2018). Cancer Genome Interpreter annotates the biological and clinical relevance of tumor alterations. *Genome Med.* **10**, 25.
- Taylor, B.S., Schultz, N., Hieronymus, H., Gopalan, A., Xiao, Y., Carver, B.S., Arora, V.K., Kaushik, P., Cerami, E., Reva, B., et al. (2010). Integrative genomic profiling of human prostate cancer. *Cancer Cell* **18**, 11–22.
- TCGA. (2015). The molecular taxonomy of primary prostate cancer. *Cell* **163**, 1011–1025.
- Teschendorff, A.E., and Zheng, S.C. (2017). Cell-type deconvolution in epigenome-wide association studies: a review and recommendations. *Epigenomics* **9**, 757–768.
- Therneau, T.M., and Grambsch, P.M. (2000). Expected Survival. In *Modeling Survival Data: Extending the Cox Model*, T.M. Therneau and P.M. Grambsch, eds. (Springer New York), pp. 261–287.
- Tomlins, S.A., Rhodes, D.R., Perner, S., Dhanasekaran, S.M., Mehra, R., Sun, X.-W., Varambally, S., Cao, X., Tchinda, J., Kuefer, R., et al. (2005). Recurrent fusion of TMPRSS2 and ETS transcription factor genes in prostate cancer. *Science* **310**, 644–648.
- Urbanucci, A., Barfeld, S.J., Kytölä, V., Itkonen, H.M., Coleman, I.M., Vodák, D., Sjöblom, L., Sheng, X., Tolonen, T., Minner, S., et al. (2017). Androgen receptor deregulation drives bromodomain-mediated chromatin alterations in prostate cancer. *Cell Rep.* **19**, 2045–2059.
- Wang, D., Garcia-Bassets, I., Benner, C., Li, W., Su, X., Zhou, Y., Qiu, J., Liu, W., Kaikkonen, M.U., Ohgi, K.A., et al. (2011). Reprogramming transcription by distinct classes of enhancers functionally defined by eRNA. *Nature* **474**, 390–394.
- Weischenfeldt, J., and Korbel, J.O. (2017). Genomes of early onset prostate cancer. *Curr. Opin. Urol.* **27**, 481–487.
- Weischenfeldt, J., Simon, R., Feuerbach, L., Schlangen, K., Weichenhan, D., Minner, S., Wuttig, D., Warnatz, H.J., Stehr, H., Rausch, T., et al. (2013). Integrative genomic analyses reveal an androgen-driven somatic alteration landscape in early-onset prostate cancer. *Cancer Cell* **23**, 159–170.

Wise, A.M., Stamey, T.A., McNeal, J.E., and Clayton, J.L. (2002). Morphologic and clinical significance of multifocal prostate cancers in radical prostatectomy specimens. *Urology* 60, 264–269.

Xing, C., Ci, X., Sun, X., Fu, X., Zhang, Z., Dong, E.N., Hao, Z.-Z., and Dong, J.-T. (2014). Klf5 deletion promotes Pten deletion-initiated luminal-type mouse prostate tumors through multiple oncogenic signaling pathways. *Neoplasia* 16, 883–899.

Yan, J., Enge, M., Whittington, T., Dave, K., Liu, J., Sur, I., Schmierer, B., Jolma, A., Kivioja, T., Taipale, M., et al. (2013). Transcription factor binding in human cells occurs in dense clusters formed around cohesin anchor sites. *Cell* 154, 801–813.

Yu, J., Yu, J., Mani, R.-S., Cao, Q., Brenner, C.J., Cao, X., Wang, X., Wu, L., Li, J., Hu, M., et al. (2010). An integrated network of androgen receptor, polycomb, and TMPRSS2-ERG gene fusions in prostate cancer progression. *Cancer Cell* 17, 443–454.

STAR METHODS

KEY RESOURCES TABLE

REAGENT or RESOURCE	SOURCE	IDENTIFIER
Antibodies		
Anti-ESRP1 rabbit polyclonal antibody	Sigma Aldrich, Germany	Atlas antibody Cat# HPA023720; RRID: AB_1856125
Anti- CD45 antibody	BioLegend, US	RRID: AB_1236444
Anti- CD326 antibody	BioLegend, US	RRID: AB_400261
Anti- CD271 antibody	BioLegend, US	RRID: AB_2282827
Anti- CD26 antibody	BioLegend, US	RRID: AB_10913814
Anti- CD31 antibody	BioLegend, US	RRID: AB_2562179
Biological Samples		
Primary and metastasis tumor samples and normal samples	This paper	
Critical Commercial Assays		
Qiagen AllPrep DNA/RNA/Protein Mini Kit		
EnVision Kit	Dako, Glostrup, Denmark	Cat#K4003
RNA6000 nano assays	Agilent	Cat#5065-4401
RNA Fragmentation Reagents	Ambion	Cat#AM8740
Deposited Data		
Raw sequencing data	This paper	EGAS00001002923
Somatic variants	This paper	https://doi.org/10.17632/6gtrxn2c.1
Software and Algorithms		
R-3.4		https://www.R-project.org
randomForestSRC 2.5.1	Ishwaran et al. (2008)	https://cran.r-project.org/package=randomForestSRC
YAPSA	Huebschmann et al. (2016)	https://bioconductor.org/packages/YAPSA/
SAMtools	Li, 2013	http://www.htslib.org/
Freebayes v1.1.0		https://github.com/ekg/freebayes
Sequenza v2.2.0.9000	Favero et al. (2015)	https://bitbucket.org/sequenza_tools/sequenza_canopy
CLICK algorithm	Sharan et al. (2003)	http://acgt.cs.tau.ac.il/expander/
Canopy 1.1.1	Jiang et al. (2016)	https://CRAN.R-project.org/package=Canopy
PEPCI	This paper	http://computational-epigenomics.com/downloads/PEPCI.R
DKFZ SNV pipeline		https://doi.org/10.1101/161638
BWA-MEM	Li (2013)	http://bio-bwa.sourceforge.net/
PCAWG delly workflow	Rausch et al. (2012)	https://github.com/ICGC-TCGA-PanCancer/pcawg_delly_workflow
LUMP algorithm	Aran et al. (2015)	www.ncbi.nlm.nih.gov/pubmed/26634437
RnBeads	Assenov et al. (2014)	https://bioconductor.org/packages/RnBeads/
EpiAnnotator	Pageaud et al. (2018)	http://epigenomics.dkfz.de/EpiAnnotator/
NNLS algorithm		https://cran.r-project.org/web/packages/nnls
Houseman algorithm	Houseman et al. (2012)	www.ncbi.nlm.nih.gov/pubmed/22568884
edgeR	Mortazavi et al. (2008); Robinson and Oshlack (2010)	http://bioconductor.org/packages/edgeR/
Genomatix software(v3.80116)		http://www.genomatix.de/
PRESCIENT	This paper	https://bitbucket.org/weischenfeldt/prescient
R package survminer v0.3.1		https://cran.r-project.org/web/packages/survminer/index.html

(Continued on next page)

Continued

REAGENT or RESOURCE	SOURCE	IDENTIFIER
R package survival v2.41-3	Therneau and Grambsch (2000)	https://cran.r-project.org/web/packages/survival/index.html
Cytoscape v3.4.0		http://www.cytoscape.org/
Other		
Cancer Genome Interpreter drug-variant list	Tamborero et al. (2018)	https://www.cancergenomeinterpreter.org/data/cgi_biomarkers_latest.zip
H3K27me3, H3K27Ac, H3K4me1, and H3K4me3 ChIP data from LNCaP cells	Barfeld et al., (2017)	https://www.ncbi.nlm.nih.gov/pubmed/28412251/
Phospho S5 RNA Pol II ChIP data	Massie et al., (2011)	https://www.ncbi.nlm.nih.gov/pubmed/21602788
H3K27me3, H3K4me1, H3K27me3 ChIP data from VCaP cells	Yu et al., (2010)	https://www.ncbi.nlm.nih.gov/pubmed/20478527
RNA pol II ChIP data from VCaP cells	Asangani et al., (2014)	https://www.ncbi.nlm.nih.gov/pubmed/24759320
Ensembl Variant Effect Predictor (VEP)		https://www.ensembl.org/info/docs/tools/vep/index.html
Exome Aggregation Consortium(ExAC)		http://exac.broadinstitute.org
IARC TP53 database		http://p53.iarc.fr/
ClinVar		https://www.ncbi.nlm.nih.gov/clinvar/
1000 Genomes Project		http://www.internationalgenome.org
NHLBI GO Exome Sequencing Project		https://esp.gs.washington.edu/drupal/
COSMIC database		http://cancer.sanger.ac.uk/cosmic/signatures
TCGA-PRAD RNA seq (Downloaded: 05 April 2017)		https://portal.gdc.cancer.gov/
TCGA-PRAD Level 3 SNP-array segmentation (Downloaded: 25 June 2018)		https://portal.gdc.cancer.gov/

CONTACT FOR REAGENT AND RESOURCE SHARING

Further information and requests for resources and reagents should be directed to and will be fulfilled by the Lead Contact, Joachim Weischenfeldt (joachim.weischenfeldt@bric.ku.dk)

EXPERIMENTAL MODEL AND SUBJECT DETAILS**Human Subjects**

Tumor samples were collected from 251 PC patients. Data was supplemented with bam files from 41 published tumor and normal WGS samples (Fraser et al., 2017). Informed consent and an ethical vote (institutional reviewing board) were obtained according to the current International Cancer Genome Consortium (ICGC) guidelines (see <http://www.icgc.org>). Manufacturing of TMAs and their analysis for research purposes as well as patient data analysis has been approved by local laws (HmbKHG, §12,1) and by the local ethics committee (Ethics commission Hamburg, WF-049/09 and PV3652). All work has been carried out in compliance with the Helsinki Declaration. Radical prostatectomy specimens were available from 17,747 patients, undergoing surgery between 1992 and 2014 at the Department of Urology and the Martini Clinics at the University Medical Center Hamburg-Eppendorf. Follow-up data were available for a total of 14,464 patients with a median follow-up of 48 months (range: 1 to 275 months).

Tissue-Microarray Processing

Archived formalin fixed tissues were used for the TMA analysis, as previously described (Kononen et al., 1998), which involved taking a 0.6 mm core from a representative tissue block from each patient. The tissues were distributed among 39 TMA blocks, each containing 144 to 522 tumor samples. For internal controls, each TMA block also contained various control tissues, including normal prostate tissue.

The usage of archived diagnostic left-over tissues for manufacturing of tissue microarrays and their analysis for research purposes as well as patient data analysis has been approved by local laws (HmbKHG, §12,1) and by the local ethics committee (Ethics commission Hamburg, WF-049/09). Informed consent was exempt based on the „Hamburgisches Krankenhausgesetz“ HmbKHG 312,1.

METHOD DETAILS

Biospecimens and Quality Control

Sample Inclusion Criteria

Biospecimens were collected from patients diagnosed with PC. Specialized pathologists dissected each prostate immediately after surgery. Dissection followed a predefined scheme to represent the position of each block relative to the entire prostate. This procedure resulted in 60 – 150 pieces of tissues depending on the size of the prostate. An image was taken from each dissected prostate specimen for later reference. After dissection, each tissue block was placed on a separately labeled cork plate covered with a special compound for cryopreservation (OCT) before the tissue was frozen to -20°C . Cryo-sections were taken from each block and presence as well as content of tumor was determined by the pathologist. The tumor cell content is given as the percentage of cancer cells relative to the entire tissue block. If necessary, IHC tumor validation (e.g. AMACR, 34BE12) was performed of the frozen tissue or after secondary paraffin embedding of selected frozen blocks. Uni- and multifocal cancers were distinguished according to the criteria of Wise et al. (Wise et al., 2002). Tumor areas were defined as part of a single focus if they were within 3 mm of each other in any section or within 4mm on adjacent sections.

Except for two patients (PCA125 and PCA176) who received pre-operation hormone therapy with LH-RH analogon, the patients did not receive any neo-adjuvant radiotherapy, androgen deprivation therapy, or chemotherapy prior to the surgical removal of tumor tissue. Tumor samples and one normal prostate control were frozen at -20°C and subsequently stored at -80°C . Eight additional normal prostate samples were obtained from a previous project (Börnø et al., 2012). DNA and RNA were extracted as described previously (Weischenfeldt et al., 2013).

ESRP1 Immunohistochemistry and FISH

TMA sections were freshly cut and used for an IHC staining performed on one day and in one experiment. The slides were deparaffinized with xylene and a descending alcohol series. Antigens were retrieved by heating for 5 minutes in an autoclave at 121°C in Tris-EDTA-Citrate buffer, pH 7.8. To prevent non-specific binding, a hydrogen peroxide blocking solution was applied for 10 minutes. The primary antibody specific for ESRP1 (rabbit polyclonal antibody, Sigma Aldrich Germany, cat#HPA023720; dilution 1:450) was incubated at 37°C for 60 minutes. The antibody (HPA023720) has been validated by the Human Protein Atlas project, which shows *i*) overlapping staining patterns with other anti-ESRP1 antibodies, *ii*) a band of appropriate size in western blots, *iii*) specific binding to ESRP1 on a protein array. The FISH probe mix consisted of a spectrum-orange labeled ESRP1 (8q22.1) probe (made from bacterial artificial chromosomes (BACs) RP11-267M23 and BAC RP11-22C11), and a spectrum-green labeled, commercial centromere 8 probe (#6J37-08; Abbott, Wiesbaden, Germany). To visualize the bound antibody, the EnVision Kit (Dako, Glostrup, Denmark) was used according to the manufacturer's directions. ESRP1 staining was found in the nucleus and cytoplasm of positive cells. In ESRP1 positive cancers, staining was usually seen in all tumor cells (100%). Hence, the staining intensity in prostate epithelial cells was estimated in four categories for each cancer, i.e. negative (not detectable), weak, moderate and strong staining.

Pathology Review

All prostate specimens were analyzed according to a standard procedure, including a complete embedding of the entire prostate for histological analysis (Erbersdobler et al., 1997). Histopathological data were retrieved from the patient's records, including tumor stage, GS, nodal stage and stage of the resection margin. PSA values were measured following surgery and PSA recurrence was defined as a postoperative PSA of 0.2 ng/ml and increasing in subsequent measurements.

Nucleic Acid Sequencing and Analysis

Whole Genome Sequencing

DNA library preparation and WGS was performed on Illumina sequencers as described earlier (Weischenfeldt et al., 2013) with a median insert size of 310 bp (sd 57 bp) and a median WGS coverage of 61-fold for tumor and 38-fold for germline control samples.

Read Alignment

WGS data was aligned to the human genome Build GRCh37 using BWA-MEM (Li, 2013) according to Pan Cancer Analysis of Whole Genomes (PCAWG) protocol (<https://doi.org/10.1101/161638>).

Median Purity

Tumor purity was calculated as the median of three purity measures, a methylation-based score defined by methylation of selected sites in the promoter of the *GSTP1* (Brocks et al., 2014), a score based on allele-specific copy number profiles (Favero et al., 2015), and a score based on the absolute quantification of somatic DNA alterations (Carter et al., 2012).

Single-Nucleotide Variant and SV Calling

Somatic SNVs were identified by the PCAWG implementation of the DKFZ SNV pipeline (<https://doi.org/10.1101/161638>). Subsequently, SNVs overlapping with tandem repeats and strand bias were marked as low-confidence and removed from the consecutive analysis.

Somatic SV discovery was pursued across all samples (matched tumor/normal genome) using the DELLY2 (Rausch et al., 2012) PCAWG analysis workflow (https://github.com/ICGC-TCGA-PanCancer/pcawg_delly_workflow). We used a high-stringency SV set by additionally filtering somatic SVs detected in $\geq 1\%$ of a set of 1105 germline samples from healthy individuals belonging to phase I

of the 1000 Genomes Project (1000 Genomes Project Consortium et al., 2015), and by removing somatic SVs present in any of the PCAWG germline samples. For inference of high-stringency SVs we further required at least four supporting read pairs with a minimum mapping quality of 20 and restricted valid somatic SV sizes from 300 bp to 500 Mb. Somatic copy number alterations (SCNAs) were identified using *sequenza* (Favero et al., 2015), which was applied to tumor and normal bam files. SCNAs near low mappability regions and with logR below 0.2 were removed. Purity parameter was selected to match the median purity (see *Median Purity* section), and ploidy parameter was selected to fit a diploid state.

We employed *freebayes* (v1.1.0) in single sample- and paired-sample calling mode for discovery of SNVs, multi nucleotide variants, and InDels < 50 bp (used parameters: `-min-repeat-entropy 1`, `-report-genotype-likelihood-max`, `-alternate-fraction 0.2`, and `-no-partial-observations`), as previously described (<https://doi.org/10.1101/208330>). Raw variant predictions were further filtered for quality (QUAL > 20, QUAL/AO > 2), strand bias artifacts (SAF > 1, SAR > 1), read position artifacts (RPR > 1, RPL > 1), and normalized for consistent representation across patients with *vt* (v0.5). Germline variants were annotated with the Ensembl Variant Effect Predictor (VEP) (r81). High impact (i.e. damaging) germline mutations were defined as frameshift, stop gain, start lost, canonical splice site, exon/gene deletions, known (ClinVar; accessed 2017-02-16) damaging non-canonical splice site variants, and somatic mosaic mutations (the latter of which are defined as mutations present in a subset of normal cells). Putative damaging germline mutations were removed if the estimated minor allele frequency (MAF) in at least one continental population was above 1%, which we judged based on 53,105 sequenced individuals that were assigned to known (control) populations and without cancer diagnosis from the ExAC resource (<http://exac.broadinstitute.org>), the 1000 Genomes Project (<http://www.internationalgenome.org>), and the NHLBI GO Exome Sequencing Project. Putative gain-of-function (GoF) missense variants in *TP53* were further evaluated based on information in the IARC TP53 database (<http://p53.iarc.fr/>) and annotated as pathogenic if *TP53* mutations were classified as “non-functional” based on experimental transcriptional activity assays. Finally, all germline mutations were excluded from the analysis if annotated as benign in ClinVar. We estimated the primary population ancestry (European, African, East Asian, South Asian, and Native American) for all patients using a supervised decomposition approach (<https://doi.org/10.1101/208330>) and ancestry-informative markers.

Copy Number Analysis

Copy number and SV profiles for each patient were binned with a 500 kb sliding bin size. Each bin containing a boolean information if an aberration occurred within the bin in the given patient. RGAs were computed by overlapping the binned data of each patient computing a cohort frequency of aberrations for each bin, and selecting the peak-frequency bins within regions with frequency higher than 5%.

Subclonal Copy-Number Analysis

Subclonal copy number were identified by computing the cancer cell fractions based on the B-allele frequency CCF_{b_i} and the depth ratio CCF_{r_i} for each segment. To compute CCF_{b_i} and CCF_{r_i} we postprocessed the DNA copy number segments following the sample-wide analysis with *sequenza*. A sample-wide analysis provides the copy number state estimate for each segment based on the total clonal contribution and the global cellularity (ρ) and ploidy (ψ) values.

We assume that subclones share the same ploidy but differ in cellularity.

Using the B-allele frequency and depth ratio models previously described (Favero et al., 2015), we used a grid search approach for each segment i to find the optimal value of the local-cellularities ρ_{b_i} and ρ_{r_i} given respectively, the observed values of B-allele frequency and depth ratio for the segment and the copy number and ploidy estimates from the sample-wide analysis.

The CCF_{b_i} and CCF_{r_i} are calculated by dividing the estimated cellularity derived by the depth-ratio model ρ_{r_i} and the B-allele frequency model ρ_{b_i} with the sample-wide cellularity ρ .

$$CCF_{b_i} = \frac{\rho_{b_i}}{\rho} \quad \text{and} \quad CCF_{r_i} = \frac{\rho_{r_i}}{\rho}$$

We then applied a bivariate Dirichlet process to generate 2D clusters CCF_{b_i} versus CCF_{r_i} . Clusters with both CCF_{b_i} and CCF_{r_i} values between 0.1 and 0.9 were identified as subclonal clusters.

Samples in which the sum of the subclonal segments represent more than 0.1% of the genome are classified as polyclonal, otherwise are classified as monoclonal.

DNA Methylation Sample Preparation and Data Analysis

Normal and tumor basal, luminal and stromal cell fractions were generated from fluorescence-activated cell sorted (FACS) cell fractions of seven BPH samples (age range 68-90) and seven PC cases (age range 55-79, GS: 3+3 (n = 3), 7 (n = 1), 4+5 (n = 1), 5+4 (n = 2)) obtained from UT Southwestern Medical Center and prepared according to (Henry et al., 2017). DNA was extracted using Qiagen AllPrep DNA/RNA/Protein Mini Kit. For the ICGC EOPC and LOPC cohorts, genomic DNA was extracted from bulk fresh frozen tumor specimen. DNA was submitted to HumanMethylation450 analyses at the Genomics and Proteomics Core Facility of the German Cancer Research Center (Heidelberg). Data quality control, preprocessing and beta-mixture inter-quantile (BMIQ) normalization was done using *RnBeads* (Assenov et al., 2014). Further data processing included removal of 27598 cross-reactive probes (Chen et al., 2013b) and 39752 sites overlapping with SNPs (dbSNP Build 150, Feb. 2017). Array-based methylation beta values were independently validated using Agena MassArray EpiTyper technology (BLUEPRINT consortium, 2016). For reference-based ct estimation, we used the Houseman algorithm (Houseman et al., 2012) with quality-controlled sorted basal, stromal, normal luminal and T-luminal cell fractions as reference cts. The fraction of infiltrating immune cells for every sample was estimated using the Leukocytes unmethylation for purity (LUMP) algorithm (Aran et al., 2015). We selected the 500 most discriminatory CpG sites between the

different cts to compute the ct composition of our EOPC samples (Figure S4B). PEPCI was calculated as the combined fraction of T-luminal cells and immune cells for every sample (Figure 5A). The computation of PEPCI was implemented in a dedicated R package (Key Resources Table).

The PEPCI R package provides quantitative information on four cts (basal, stromal, normal luminal and T-luminal cells) and infiltrating immune cells, inferred from methylation data. The PEPCI score represents the combined percentage of T-luminal and immune cells as a measure of tumor aggressiveness.

Ct-specific reference methylomes are used to estimate ct composition in bulk tumor samples, employing the Houseman algorithm, which is a common tool to deconvolute the composition of blood samples. The algorithm selects a specified number of CpG sites with most variable methylation between provided reference cts. This process is predefined in the PEPCI R package, which processes Illumina 450k or EPIC array data and interrogates 500 preselected CpG sites. The location of these sites relative to ChromHMM states of prostate epithelial cells indicates significant enrichment of T-luminal cell hypermethylation in promoter CpG islands, and stromal-specific hypermethylation in enhancer regions (Figure S4C, heatmap legend on the right).

Methylation based principal component analysis was done using RnBeads (Assenov et al., 2014). Enrichment of CpG sites at chromatin states was performed with EpiAnnotator (Pageaud et al., 2018), using ChromHMM states for prostate epithelial cells (Taberlay et al., 2014). Trees representing sample similarities were constructed from methylation-based Euclidean pairwise distances using the algorithm for phylogenetic tree reconstruction of Desper and Gascuel (Desper and Gascuel, 2002). Logistic regression models based on methylation data and their evaluations using receiver operating characteristic (ROC) curves were performed using the R programming language.

Heterogeneity estimates of heterogeneity and multifocal cases were calculated by averaging all pairwise dissimilarities between methylation-based ct fractions of the corresponding multi-area samples using cosine dissimilarity.

For the TCGA PRAD cohort, HumanMethylation450 raw signal intensities of probes for each participant's tumor sample (n = 498) were downloaded as idat files from the TCGA data portal (<https://tcga-data.nci.nih.gov>) and processed as described for the ICGC cohort.

Tri-Nucleotide Mutational Signature

To identify mutational signatures, we applied YAPSA (Yet Another Package for Signature Analysis) (Huebschmann et al., 2016), a linear combination decomposition of the mutational catalog with predefined signatures from the COSMIC database (<http://cancer.sanger.ac.uk/cosmic/signatures>, downloaded June 2016) computed by non-negative least squares (NNLS). To increase specificity, the NNLS algorithm was applied twice; after the first execution, only those signatures whose exposures, i.e. contributions in the linear combination, were higher than a certain cut-off were kept, and the NNLS was run again with the reduced set of signatures. As the detectability of different signatures may vary, signature-specific cut-offs were determined in a random operator characteristic analysis using publicly available data on mutational catalogs of 7,042 cancers (507 samples with WGS; 6,535 samples with whole exome sequencing) (Alexandrov et al., 2013) and mutational signatures from COSMIC. This yielded the following signature-specific cutoffs: AC1: 0; AC2: 0.01045942; AC3: 0.08194056; AC4: 0.01753969; AC5: 0; AC6: 0.001548535; AC7: 0.04013304; AC8: 0.242755; AC9: 0.1151714; AC10: 0.01008376; AC11: 0.09924884; AC12: 0.2106201; AC13: 0.007876626; AC14: 0.1443059; AC15: 0.03796027; AC16: 0.3674349; AC17: 0.002647962; AC18: 0.3325386; AC19: 0.1167454; AC20: 0.1235028; AC21: 0.1640255; AC22: 0.03102216; AC23: 0.03338659; AC24: 0.03240176; AC25: 0.01611908; AC26: 0.09335221; AC27: 0.009320062; AC28: 0.05616434; AC29: 0.05936213; AC30: 0.05915355. We removed mutation signature present in fewer than 10% of the samples.

Knowledge-Based Analysis of APOBEC-Associated Mutational Processes

Enrichment and mutation load associated with APOBEC mutagenesis were calculated based on prior mechanistic knowledge about mutation motifs associated with certain mutagenic factors and pathways (Chan et al., 2015; Roberts and Gordenin, 2014). Calculations were done for genome-wide mutation calls and for mutation calls only in C/G clusters identified as described in (Chan et al., 2015; Roberts et al., 2012). Briefly, the enrichment with a tri- or tetra-nucleotide motif $pXq \rightarrow pZq$ were calculated, where X is the mutated nucleotide, Z is the nucleotide after base substitution, p is the -1 nucleotide (or -1 and -2 nucleotides), and q is the +1 nucleotide (within the context of the given mutation type/ trinucleotide). For each motif, we also included the reverse complement sequence that would represent the mutagenic process occurring on the opposite DNA strand. To statistically evaluate whether a certain mutation type is enriched in a sample as compared to mutations generated by random mutagenesis, a one-sided Fisher's exact test was performed. To account for multiple testing, p values obtained were corrected using the Benjamini-Hochberg method.

The MAF of the germline APOBEC3B deletion in our PC cohort was 7.0%, in line with the expected frequency in individuals with a European germline genetic background.

RNA-seq Sample Preparation and Data Analysis

RNA extraction and sequencing for the samples ICGC_PCA1-12 was performed as described in a previously publication (Weischenfeldt et al., 2013). DNase digested total RNA from additional 109 EOPC samples and 9 control samples was analyzed using RNA6000 nano assays (Agilent 2100 Bioanalyzer) and Qubit 2.0 Fluorometer. Only samples with an RNA Integrity Number (RIN) > 7.0 were included in this study. We used 1-4 micrograms of total RNA from each sample to prepare Truseq stranded sequencing libraries (Illumina). In brief, poly-A enrichment, fragmentation, first and second strand synthesis, A-tailing, and adapter ligation were performed following the manufacturer's instructions. Libraries were PCR-amplified for 7-20 cycles and qualitatively validated on an Agilent 2100 Bioanalyzer of product size and concentration and on Qubit. Libraries were sequenced 50 bp paired-end on a HiSeq 2000 flowcell according to Illumina's protocol.

RNA reads were aligned to hg1000 using BWA (v. 0.5.9-r16 for reads up to 51 bases and v. 0.7.7-r441 for reads with 100 bases) and SAMtools. Uniquely mapped reads were annotated using Ensembl v62. Gene expression levels were quantified in reads per kilobase of exon per million mapped reads (RPKM) and corrected for RNA composition effects applying TMM implemented in the R package edgeR (Mortazavi et al., 2008; Robinson and Oshlack, 2010). Multi-area samples of the same patient were merged in to an artificial sample by taking the sum of read counts per gene before RPKM calculation resulting in a cohort of 96 RNA-seq samples. Hierarchical clustering on the most variable genes revealed batch effects across the RNA-seq cohort. Using hierarchical clustering and sample preparation information, a set of 42 tumor RNA-seq samples without batch effects was manually selected and used to identify co-expression clusters applying the algorithm CLICK, part of the software tool EXPANDER (v7.11) (Sharan et al., 2003). CLICK was run with default parameters on \log_2 transformed and z-score normalized RPKM values of the 1231 most variable genes. Genes were expressed in minimum 3 samples ≥ 0.5 RPKM. 14 CCs were identified showing an overall separation of -0.039 and overall homogeneity of 0.632. Seven out of 14 CCs showed a homogeneity value ≥ 0.6 and were selected for further analyses (named CC1-CC7). An 8th CC also showed a high homogeneity value, but consisted mainly of one protocadherin gene cluster and was discarded. We calculated a mean pattern value for each CC in each of the EOPC samples. A mean pattern value for one sample is defined by taking the trimmed mean across \log_2 and z-score transformed RPKM values of genes in a particular CC. Based on the mean pattern values obtained for each CC, tumor samples were divided into two subgroups (called CC-high and CC-low) using partitioning around medoids (pam). We compared the subgroups in an CC using edgeR and selected differentially expressed genes following the expression pattern in a CC with $|\log_2(\text{FC})| \geq \log_2(2)$, $\text{FDR} \leq 0.01$ and difference of median expression > 1 , resulting in overall 417, 282, 189, 176, 117, 96, 86 and 21 genes in CC1-CC7, respectively (Table S4). After the establishment of the CCs, the remaining 54 EOPC RNA-seq samples were reintegrated. Mean pattern and CC subgroups were recalculated as described above taking the whole RNA-seq cohort of 96 samples (Table S4). CCs were functionally annotated applying gene set overrepresentation analysis of the GePS Genomatrix software (v3.80116). For additional annotation and comparison of the CCs to the literature, we integrated external signatures that are associated with high risk PC (BROMO10), Gleason score, stroma or reactive stroma into the mean pattern matrix (Jhun et al., 2017; Planche et al., 2011; Stuart et al., 2004; Urbanucci et al., 2017).

RPKM values for the TCGA cohort (495 samples) were calculated as described above. Batches with the ID 312 and 320 were excluded due to batch effects resulting in a cohort of 462 samples. To classify TCGA samples into CC subgroups, RPKM values were log transformed and z-score normalized, and mean pattern values for each sample and CC were calculated. Based on the mean pattern values, samples were assigned to the CC subgroup with nearest medoid. Here, the medoids originate from the calculations on the ICGC EOPC cohort.

In TCGA, subgroup 1 (97 samples) and subgroup 3 (143 samples) could be derived from the hierarchical clustering using the same features as in our ICGC EOPC cohort. To annotate subgroup 2 in the TCGA data, we applied criteria defined from our ICGC EOPC cohort. As described above, the samples belonging to the “Immune” subgroup showed a high immune cell content and high expression of CC5 and CC7. Here, the lowest immune cell content in subgroup 2 ranked at the 94th percentile considering a normal distribution, and the mean and standard deviation of the estimated immune cell content across the 96 EOPC samples with RNA-seq. In total nine TCGA samples were assigned to subgroup 2 based on high PEPCI score, CC5-high and CC7-high, and a high immune cell content defined by the 94th percentile of immune cell content values.

Before the comparison of subtype fractions in ICGC EOPC, TCGA EOPC (100 cases) and TCGA LOPC (360 cases), GS composition differences were adjusted to the ICGC EOPC cohort (fractions of GS in ICGC: GS6 = 0.135, GS7 = 0.72, GS8 = 0.01, GS > 8 = 0.135). The GS-corrected subtype fractions in the TCGA EOPC and TCGA LOPC cohorts were calculated using 1,000 bootstrap samples. A single resampling was performed by extracting TCGA EOPC/LOPC cases according to the GS, and by drawing a bootstrap sample of these cases for each GS (GS6, GS7, GS8, GS > 8) independently. Here, the sample size of a GS bootstrap in TCGA related to the GS fraction in ICGC EOPC (e.g. for GS6 and TCGA LOPC the sample size is equal to $360 \cdot 0.135$). From the GS-corrected bootstrap samples the fraction of subgroups was calculated. The p value of the differences in subgroup fraction was based on a permutation test.

Based on gene expression, the heterogeneity of multi-area samples belonging to the same patient was estimated by taking the average of the pairwise dissimilarity values between multi-area samples. To calculate the pairwise dissimilarity values we took the mean of the cosine dissimilarity between multi-area samples in the different CCs. Here, the cosine dissimilarity was measured across the gene expression values of a particular CC.

Breakpoint-Association with Chromatin Data

Chromatin-related data from PC tissue and cell lines were downloaded from different studies to generate chromatin states (ChromHMM). ChromHMM from normal prostate epithelial cells PrEC and PC3 cells were downloaded from GSE57498. Similar 9 ChromHMM states were produced for LNCaP and VCaP cells using ChromHMM software (Ernst and Kellis, 2012). To learn ChromHMM states in LNCaP cells we computed H3K27me3, H3K27Ac, H3K4me1, and H3K4me3 profiles (Barfeld et al., 2017), CTCF binding profile (ENCODE), and Phospho S5 RNA Pol II binding profile (Massie et al., 2011). For VCaP cells we computed H3K27me3, H3K4me1, H3K27me3 (Yu et al., 2010), RNA pol II profiles (Asangani et al., 2014), and CTCF and H3K27Ac profiles (ENCODE). The resulting 9 chromatin states for PrEC, PC3, LNCaP, and VCaP cells were reduced to 7 by combining “enhancer+CTCF” and “promoter+CTCF” states together with “enhancer” and “promoter”, respectively. The derived 7 ChromHMM states were then used to annotate DNA methylation data. For enrichment analysis of DNA breaks we excluded the states “transcribed” and “bound by CTCF”. SV breakpoints were also tested for overlap with LNCaP GRO-seq (Wang et al., 2011; Chae et al., 2015), FAIRE-seq peaks from LNCaP and VCaP (Urbanucci et al., 2017), general super-enhancers (Hnisz et al., 2013), ETV1 ChIP

peaks from LNCaP cells (Chen et al., 2013a), ERG ChIP peaks from VCaP cells (Yu et al., 2010), BRD4 ChIP peaks from VCaP cells (Asangani et al., 2014) and PC-specific super-enhancers (Kron et al., 2017).

SV breakpoints from EOPC and LOPC samples were assessed by performing intersection between chromatin states and SV breakpoints using bedtools v2.25.0 (Quinlan and Hall, 2010), adding 5 kbp to both sides of the peaks. To compute an expected overlap frequency, breakpoints were randomly shuffled 100 times on the genome (excluding telomere and centromere regions, downloaded from UCSC, hg19) and keeping the SV size and chromosome fixed before performing overlap.

Association of SVs with DNA-DNA interaction and open chromatin marks was measured in a correlation-based analysis between breakpoint density and marks of physically interacting and open chromatin. We divided the genome in 1 Mb sliding windows using a 100 kb step and overlapped each bin with the SV breakpoints, retaining maximum 1 overlap per patient per bin, the number of chromatin loops and PC-specific H3K27ac peaks. Spearman's Rho was estimated by correlating the EOPC and LOPC breakpoints with the number of Hi-C loops and H3K27ac peaks, respectively.

For Hi-C, we combined the loop annotations from 8 human cell-lines (GM12878, Hela, HMEC, HUVEC, IMR90, K562, KBM7, NHEK), obtained from GSE63525 (Durand et al., 2016; Rao et al., 2014), and removed duplicate chromatin loops. H3K27ac PC-specific peaks were obtained from (Kron et al., 2017).

Exclusion Score Estimate

Here we define Exclusion score (E) as a metric to evaluate the preference of an aberration to occur as a sole event, or in tandem with many aberrations.

For every patient x , we construct an aberration index A_x that contains a list of all the $I_i(x)$ deleted genes/regions for that patient, e.g. $A_x = \{BRCA1, ERG, ELK4\}$. The exclusion score is defined as the fraction of the observed aberration, in this case 1, and the total number of aberrations for that patient:

$$E_i(x) = \frac{1}{|A_x|}, i \in A_x$$

The exclusion score for a given aberration i , is defined as the mean exclusion score across all patients:

$$E_i = \frac{1}{N} \sum_{n=1}^N E_i(n)$$

The exclusion score is confined between 0 and 1 and the interpretation is such that, the higher the exclusion score of an aberration, the more frequently it tends to occur as a single event or in combination with very few events and vice versa.

Pairwise Exclusion Score

In a similar manner we can compute the exclusion score for a pair of aberrations i and j which is the "preference" of that pair to occur with few or many over events,

$$E_{ij}(x) = \frac{2}{|A_x|}, i, j \in A_x$$

and compute the mean pairwise exclusion score respectively,

$$E_{ij} = \frac{1}{N} \sum_{n=1}^N E_{ij}(n)$$

Survival Analysis

We employed Random Survival Forests (RSF) to predict the PEFS, using the time (in months) from diagnosis to BCR as the response variable. The model was implemented in R using the randomForestSRC package (Ishwaran et al., 2008), with n.tree = 5,000. Missing data were imputed each time a tree node performed a split on samples with missing values. Split statistics were aggregated over all trees to determine the median split value for each variable (PEPCI 69.1). We chose a random forest approach to binarize the PEPCI-score since it is able to treat continuous right-censored survival data and identify the optimal split that separates the samples into high and low risk groups.

For BCR analyses incorporating GS, samples were grouped into the categories GS6, GS3+4, GS4+3 and GS8-10 for ICGC, and GS6, GS3+4, GS4+3 and GS8, GS9-10 for TCGA. In ICGC, only one case showed GS8 and therefore included into the GS9-10 group. Time to BCR was right-censored at 100 months for TCGA PRAD. Prediction of BCR was analyzed using Kaplan-Meier curves and log-rank test, and cox proportional hazards regression model (CPHM). Fitted CPH models were compared using log-likelihood ratio test. Here, we tested a full model incorporating GS, and the introduced PEPCI groups, CC2/CC7 groups or subgroups against a model incorporating GS only. All analyses were done using R (R-3.3.3) and the R packages survminer (v0.3.1) and survival (v2.41-3) (Therneau and Grambsch, 2000). CPHM and LRT related results were provided in Table S4.

We assessed the predictive advantage of *ESRP1* gain over *MYC* gain by comparing the variable importance (VIMP) values of the two features in a RSF model, using PSA, pT, GS, Age, CC2, and PEPCI, to predict BCR. We trained 1,000 models to get the VIMP distribution of *ESRP1* and *MYC*. A one-sided Wilcoxon test shows that VIMP associated with *ESRP1* gain is significantly higher than *MYC* gain (p value < 2.2e-16)

PRESCIENT Tumor Evolution Model

PRESCIENT (<https://bitbucket.org/weischenfeldt/prescient>) uses conditional probability to predict the order of molecular events, given a known or observed co-occurrence matrix. It differs from similar algorithms previously published including CAPRI (Ramazzotti et al., 2015) and TO-DAG (Lecca et al., 2015) by the ability of predicting the next event in a progressive manner rather than compute an overall general consensus evolution tree, and use the estimate of event free survival to predict patient outcome based on genomic evolution. Additionally it includes a novel metric, Exclusivity Score, which measure the tendency of an aberration to occurs with other events.

PRESCIENT is based on the following assumptions i) molecular events that are often observed in the same tumor are more likely to be phylogenetically closely related ii) molecular event(s) that are often observed as the exclusive events, are more likely to occur early in the tumor evolution. As molecular events, we used the RGAs and used the presence or absence in each patient to generate a co-occurrence matrix. PRESCIENT constructs an expected frequency distribution $F(f)$ to identify the most probably initiating RGA event. The RGA co-occurrence matrix is bootstrap sampled 10,000 times, and at each iteration, a new exclusion score matrix and RGA co-occurrence frequency matrix is computed. The co-occurrence and exclusion score matrices were used to compute the $P(f)_i$ and $P(e)_i$ for each RGA respectively, and the probability $P_i = P(f)_i P(e)_i$ of an RGA i to occur. The first event in the branch corresponds to the event with the highest probability P_i . This RGA is then removed from the RGA co-occurrence matrix, and the resulting subset is used to recompute a new $P(f)_i$ and $P(e)_i$ for each remaining RGA. The same approach is applied to assign the following RGA in the branch until no events are left in the resulting RGA co-occurrence matrix. Each permutation yields a putative evolution trajectory formed by an ordered series of events.

PRESCIENT associates a probability score for each node in the trajectory. Using these precomputed trajectories, PRESCIENT can take as input a set of RGAs detected in a patient, to predict the most probable next RGAs in the trajectories of the patient and the associated patient disease progression.

Clonal Reconstruction

Clonal reconstruction was done for multi-region tumors. To identify the clonal evolution from tumor samples with multiple sequenced tumor regions, we applied the R package Canopy (Jiang et al., 2016), using default parameters. As input for the reconstruction, we used nsSNVs, tumor/normal depth ratio and allele frequency information from sequenza (https://bitbucket.org/sequenza_tools/sequenza_canopy). Reconstructed evolution trees were curated following the guidelines in the R package documentation.

PRESCIENT Method Validation

From a cohort of 40 patients with 30x WGS primary PC and local lymph node metastasis, we estimated the phylogenetic trees for each patient as described in the heterogeneity cases (with Canopy).

The PRESCIENT method was compared to a naive-frequency approach, in which each RGA have the probability of occurrence given by its frequency in the cohort.

We tested the ability to predict the next RGA in the phylogeny, which served as a true positive set. To compute a true positive prediction, PRESCIENT prediction and the frequency-based prediction were compared to the observed RGA for every node in the tree. A false-positive set was calculated using both methods, by extracting the most abundant RGA in the cohort, which was not present in the patient.

To further assess the robustness of the method, we compared the main evolution trajectory predicted by PRESCIENT with the estimated probability of the same trajectory calculated by random subsampling (10% of the dataset, 10,000 times). We found overall highly similar probabilities, with random-subsampling based probability of the first node within 1.5 standard deviations from PRESCIENT prediction and 1.55 for the second node.

Drug-Variant Targets

Drug-variants were downloaded from <https://www.cancergenomeinterpreter.org> (April 15, 2018) (Tamborero et al., 2018). Germline SNP, somatic SNV, SCNA and SV variant types were matched with Biomarker types (e.g. a Biomarker fusion type was matched with SV-mediated fusions and Biomarker deletion matched with SCNA deletion in our dataset). All predicted damaging germline PTVs were considered irrespective of the Biomarker amino acid change. Only Biomarkers associated with a Responsive effect and in pre-clinical or clinical trial or currently in clinical guidelines for PC were considered. BRCAness was scored as tumor genomes with at least 40% contribution of mutation signature 3 and minimum 1,000 somatic SNVs.

QUANTIFICATION AND STATISTICAL ANALYSIS

Quantification and statistical analysis methods are described in the [STAR Methods](#) detail subsections.

DATA AND SOFTWARE AVAILABILITY

The accession number for WGS, RNA-seq expression and array-based methylation reported in this study is EGA: EGAS00001002923. Somatic variant calls are available through Mendeley Data <https://doi.org/10.17632/6gttrxrnr2c.1>. Oncological outcome data were collected via the Progether PROM's (patient reported outcome measurement) interface (www.progether.com/proms) and the martini-clinic database.

Softwares used for each analysis are described and referenced in [Methods Details](#) subsection and listed in [Key Resource Table](#).